The caveolin–cavin system plays a conserved and critical role in mechanoprotection of skeletal muscle

Harriet P. Lo,[1] Susan J. Nixon,[1] Thomas E. Hall,[1] Belinda S. Cowling,[3] Charles Ferguson,[1,2] Garry P. Morgan,[2] Nicole L. Schieber,[1] Manuel A. Fernandez-Rojo,[1] Michele Bastiani,[1] Matthias Floetenmeyer,[1,2] Nick Martel,[1] Jocelyn Laporte,[3] Paul F. Pilch,[4] and Robert G. Parton[1,2]

[1]Institute for Molecular Bioscience and [2]Center for Microscopy and Microanalysis, The University of Queensland, Brisbane, Queensland 4072, Australia
[3]Department of Translational Medicine and Neurogenetics, Institut de Génétique et de Biologie Moléculaire et Cellulaire, Institut National de la Santé et de la Recherche Médicale U964, Centre National de la Recherche Scientifique UMR7104, Strasbourg University, Illkirch 67404, France
[4]Department of Biochemistry, Boston University School of Medicine, Boston, MA 02118

Dysfunction of caveolae is involved in human muscle disease, although the underlying molecular mechanisms remain unclear. In this paper, we have functionally characterized mouse and zebrafish models of caveolae-associated muscle disease. Using electron tomography, we quantitatively defined the unique three-dimensional membrane architecture of the mature muscle surface. Caveolae occupied around 50% of the sarcolemmal area predominantly assembled into multilobed rosettes. These rosettes were preferentially disassembled in response to increased membrane tension. Caveola-deficient *cavin-1*$^{-/-}$ muscle fibers showed a striking loss of sarcolemmal organization, aberrant T-tubule structures, and increased sensitivity to membrane tension, which was rescued by muscle-specific Cavin-1 reexpression. In vivo imaging of live zebrafish embryos revealed that loss of muscle-specific Cavin-1 or expression of a dystrophy-associated Caveolin-3 mutant both led to sarcolemmal damage but only in response to vigorous muscle activity. Our findings define a conserved and critical role in mechanoprotection for the unique membrane architecture generated by the caveolin–cavin system.

Introduction

The sarcolemma of skeletal muscle represents one of the most specialized plasma membrane systems known in mammalian cells. The two most striking features of the sarcolemma are caveolae, which cover the entire cell surface, and the T-tubules, which form an elaborate plasma membrane–connected system of fine tubules that penetrate into the center of the muscle fiber. Early morphological studies suggested that T tubules link to the sarcolemma through sarcolemmal caveolae, potentially acting as a barrier to maintain distinct lipid and protein compositions of the T-tubule system (Rayns et al., 1968). Both caveolae and T tubules have been linked to caveolin-3 (Cav3), the major membrane protein of skeletal muscle caveolae (Way and Parton, 1995; Parton et al., 1997). Mutations in the gene for Caveolin-3 (*CAV3*) are associated with various human muscle diseases, including limb-girdle muscular dystrophy type 1C (LGMD1C) and rippling muscle disease (RMD; Woodman et al., 2004), and a loss of Cav3 perturbs sarcolemmal caveolae and T-tubule formation in both humans and mice (Galbiati et al., 2001; Minetti et al., 2002). Morpholino (MO)-based knockdown of Cav3 in the zebrafish also demonstrated a role for Cav3 in myoblast fusion (Nixon et al., 2005). Cav3/caveolae clearly play an important (although not essential) role in T-tubule biogenesis, and it has been suggested that the propagation of silent action potentials through the abnormal T-tubule system may be the underlying cause of RMD (Lamb, 2005). The interaction of Cav3 with dysferlin, a sarcolemmal protein implicated in membrane fusion, further raises the possibility of a role in the membrane repair process (Matsuda et al., 2001; Bansal et al., 2003). These studies highlight the importance of Cav3 and caveolae in general for muscle development and physiology. However, the molecular mechanisms that underlie the significance of caveolae in human muscle pathologies remain poorly understood.

The discovery of the cavin family of proteins that regulate caveola formation and stabilization has provided new avenues to understand the role of muscle caveolae. Cavin-1 (also known as PTRF), Cavin-2 (SDPR), Cavin-3 (SRBC), and Cavin-4 (MURC) are components of a coat complex associated with caveolae (Bastiani and Parton, 2010). Cavin-1

Correspondence to Robert G. Parton: R.Parton@imb.uq.edu.au

M. Floetenmeyer's present address is Max-Planck-Institute for Developmental Biology, 72076 Tuebingen, Germany.

Abbreviations used in this paper: AAV, adeno-associated virus; DHPR, dihydropyridine receptor; DIC, differential interference contrast; EBD, Evans blue dye; FDB, flexor digitorum brevis; hpf, hour postfertilization; HYB, hybridization buffer; MC, methylcellulose; MO, morpholino; PLA, proximity ligation assay; RMD, rippling muscle disease; WT, wild type.

The Rockefeller University Press $30.00
J. Cell Biol. Vol. 210 No. 5 833–849
www.jcb.org/cgi/doi/10.1083/jcb.201501046

is essential in caveola formation and organization and is expressed in all cells possessing caveolae where it associates with Caveolin-1 (Cav1) or Cav3 to drive caveola formation in nonmuscle and muscle cells, respectively (Hill et al., 2008; Liu and Pilch, 2008b). Patients lacking Cavin-1 lose skeletal muscle caveolae and have decreased Cav3 protein levels, accompanied by muscular dystrophy and generalized lipodystrophy (Hayashi et al., 2009). Cavin-1 has also been implicated as a docking protein together with MG53 during acute cell damage and membrane repair (Zhu et al., 2011). Furthermore, Cavin-4 is the muscle-specific cavin family member and interacts with Cavin-1 and Cavin-2 as well as components of the RhoA–Rho-associated kinase (ROCK) signaling pathway, leading to stimulation of the serum response factor receptor and subsequent transcriptional activation of atrial natriuretic peptide (Ogata et al., 2008; Bastiani et al., 2009). Although the role of Cavin-4 in skeletal muscle has not yet been defined, overexpression of Cavin-4 leads to cardiac dysfunction and enlarged caveolae in a transgenic mouse model (Ogata et al., 2008, 2014), and mutations in *cavin-4* have been implicated in dilated cardiomyopathy (Rodriguez et al., 2011).

The involvement of caveolar components in human muscle disease emphasizes their importance in muscle development and function. Accumulating evidence suggests a role for caveolae in mechanotransduction or as a membrane reservoir to minimize increases in membrane tension when the cell surface is subjected to mechanical force. Myotubes expressing mutant Cav3 demonstrate increased membrane fragility, and fibroblast caveolae flatten in response to hypotonic medium releasing Cav1 into the bulk membrane and Cavin-1 into the cytosol (Sinha et al., 2011). A caveolae-dependent membrane reservoir model is particularly attractive for the myofiber, which undergoes rounds of membrane stretching and contraction, and the myofiber provides an excellent system to examine the effect of defined changes in the plasma membrane on caveolae.

To date, a substantial number of muscle function and disease model studies have used cultured myotubes. Although these studies have been advantageous in aiding the understanding of skeletal muscle physiology, it is important to note that cultured myotubes lack the structure and characteristics of mature skeletal muscle fibers (Ravenscroft et al., 2007). On the contrary, the use of enzymatically dissociated muscle fibers from the flexor digitorum brevis (FDB) of rodents is a well-established technique and represents a more accurate method for in vitro modeling of mature skeletal muscle. Therefore, we have used both whole muscle and the FDB-isolated muscle fiber system from mature wild-type (WT) and Cavin-1–null mice together with quantitative and 3D EM and functional experiments to address the role of caveolae in sarcolemmal organization and membrane stability of adult muscle. We further used the zebrafish model for muscle-specific Cavin-1 knockdown to study the effects of a loss of muscle caveolae. Our findings reveal an integral role for the caveolar membrane microdomain in stabilizing the muscle fiber surface. A loss of caveolae as a result of Cavin-1 deficiency compromises sarcolemmal integrity in response to both experimental mechanical stress and high physiological muscle activity, highlighting the caveolin–cavin system as an essential mechanoprotective element of the plasma membrane in skeletal muscle.

Results

Loss of Cavin-1 recapitulates aspects of the skeletal muscle phenotype observed in patients

In this study, we used the *cavin-1*$^{-/-}$ mouse model, which lacks caveolae in all tissues (Liu et al., 2008a). Histological analysis of WT and *cavin-1*$^{-/-}$ skeletal muscle revealed only mild histological changes, with centralized nuclei indicative of muscle regeneration present in 7% of *cavin-1*$^{-/-}$ muscle fibers (compared with 1% in WT muscle; Fig. 1, A and B). To test overall muscle strength, *cavin-1*$^{-/-}$ mice were subjected to a hanging test by measuring the length of time each mouse could grip an inverted mesh screen. *Cavin-1*$^{-/-}$ mice had significantly reduced hang times, recording a mean hang time of 0.3 min compared with 3.1 min in WT mice (Fig. 1 C and Video 1). We further evaluated the effects of Cavin-1 deficiency on muscle function using forced treadmill running to analyze both endurance capacity and maximum speed. Exercise endurance capacity was moderately (but significantly) reduced in *cavin-1*$^{-/-}$ mice (mean running distance of 788.4 m compared with 871.9 m in WT; Fig. 1 D). There was no significant difference in maximum speed between WT and *cavin-1*$^{-/-}$ mice (Fig. 1 E). Although these tests may not represent a strictly muscle defect, they do nonetheless suggest an overall reduced muscle function in the *cavin-1*$^{-/-}$ mouse. However, collectively with the previously characterized lipodystrophy phenotype (Liu et al., 2008a), our findings suggest that *cavin-1*$^{-/-}$ mice recapitulate the phenotypes reported in Cavin-1–deficient patients (Hayashi et al., 2009).

Loss of Cavin-1 results in prominent sarcolemma, T-tubule, and endomembrane abnormalities

We next examined the ultrastructural organization of WT and *cavin-1*$^{-/-}$ muscle fibers using ruthenium red to demarcate surface-connected membrane systems. WT muscle fibers at low magnification showed a generally straight sarcolemma but with abundant caveolae; glancing sections revealed that caveolae were organized into striking rosette-like structures (Fig. 1, F and G). EM stereological techniques and quantitative tomography revealed that caveolae provided up to half of the surface area in WT muscle fibers (Fig. 1 I).

By comparison, the sarcolemma of *cavin-1*$^{-/-}$ muscle fibers was characterized by a lack of caveolae and a strikingly irregular and convoluted appearance (Fig. 1 H). Muscle sections from the gastrocnemius of *cavin-1*$^{-/-}$ adult mice showed a similar convoluted sarcolemma in contrast to WT muscle tissue (Fig. S1 A). One of the most prominent features of *cavin-1*$^{-/-}$ muscle fibers was the abundance of abnormal surface-connected vacuoles (Fig. 2), which had a larger and more irregular diameter than caveolae (equal to a 4.2-fold difference in mean surface area; Fig. S2 A). However, quantitation of the relative surface area in WT and *cavin-1*$^{-/-}$ fibers revealed that the surface area provided by the vacuoles was similar to that provided by caveolae (Fig. 1 I). Therefore, despite the ultrastructural abnormalities observed, the loss of caveolae is not correlated to a loss of surface area (relative to the sarcomere unit). An additional feature of the peripheral region of *cavin-1*$^{-/-}$ muscle fibers was the presence of multilamellar vacuolar structures (Fig. S2 B).

We next examined the organization of the T-tubule system in the WT and *cavin-1*$^{-/-}$ muscle fibers. T-tubule dysmor-

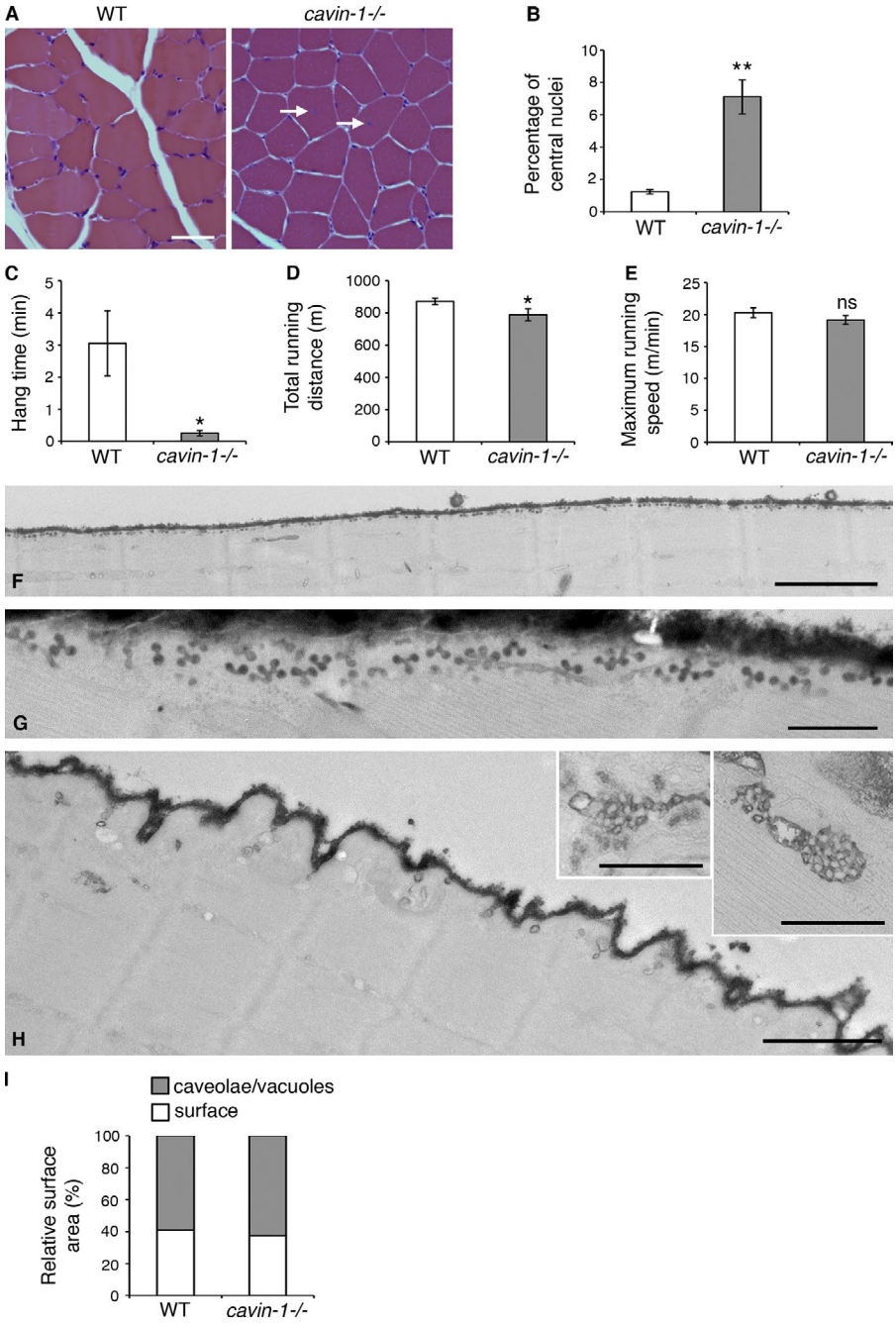

Figure 1. **Loss of Cavin-1 in mice recapitulates the skeletal muscle phenotype observed in patients.** (A) Hematoxylin and eosin staining of WT and *cavin-1*$^{-/-}$ muscle sections. Arrows indicate centralized nuclei in *cavin-1*$^{-/-}$ muscle sections. Bar, 50 µm. (B) WT muscle has 1.2 ± 0.1% central nuclei compared with 7.1 ± 1.1% central nuclei in *cavin-1*$^{-/-}$ muscle (determined by counting number of central nuclei in 564 and 596 muscle fibers from three pairs of WT and *cavin-1*$^{-/-}$ mice, respectively). No further changes in histology were observed in *cavin-1*$^{-/-}$ mice up to 20 mo of age (not depicted). (C–E) WT and *cavin-1*$^{-/-}$ mice were tested for hang time (C), endurance capacity (D), and maximum running speed (E). WT mice had a mean hang time of 3.1 ± 1.0 min compared with 0.3 ± 0.1 min in *cavin-1*$^{-/-}$ mice. Use of the holding impulse (hang time × body weight) measurement to correct for effects of body mass on hang time yielded the same results (not depicted). Exercise endurance capacity, measured as total running distance before exhaustion, was 871.9 ± 20.6 m in WT mice and 788.4 ± 37.6 m in *cavin-1*$^{-/-}$ mice. Maximum running speed was 20.3 ± 0.8 m/min in WT mice and 19.2 ± 0.7 m/min in *cavin-1*$^{-/-}$ mice. Tests performed on 10 WT and 6 *cavin-1*$^{-/-}$ mice. Error bars show means ± SEM. *, $P \leq 0.05$; **, $P \leq 0.01$; ns, not significant. (F–H) Ruthenium red–labeled isolated FDB fibers from WT (F and G) and *cavin-1*$^{-/-}$ (H) mice show the convoluted surface of caveola-deficient *cavin-1*$^{-/-}$ fibers, in contrast to the straight sarcolemma of WT fibers decorated by rosettes of uniform surface-connected caveolae. Insets show reticular networks characteristic of immature Cav3-positive structures (Parton et al., 1997). Bars: (F) 2 µm; (G and H, insets) 0.5 µm; (H, main image) 2 µm. (I) Quantitation of sarcolemmal features in WT and *cavin-1*$^{-/-}$ fibers. Unit of muscle membrane (micrometers) per sarcomere is expressed as a proportion (percentage) occupied by sarcolemmal surface excluding caveolae (in WT) and surface-connected vacuoles (in *cavin-1*$^{-/-}$). Sarcolemmal surface occupies 41% and 37% in WT and *cavin-1*$^{-/-}$ in muscle fibers, respectively (unshaded). Caveolae occupy 59% of the sarcolemma in WT muscle fibers, whereas vacuoles occupy 63% of the sarcolemma in *cavin-1*$^{-/-}$ muscle fibers (shaded gray). Note that stereological measurements have not been corrected for overprojection effects (see Materials and methods).

phology has been observed in Cav3-deficient mice and humans (Galbiati et al., 2001; Minetti et al., 2002). In WT muscle fibers, surface connected T-tubules were apparent, running in normal transverse orientation adjacent to the Z lines (Fig. 2, A and B). In contrast, regions of the subsarcolemmal T-tubule system were more irregular in *cavin-1*$^{-/-}$ muscle fibers, with increased longitudinal elements. Peripheral elements were also often dilated in the *cavin-1*$^{-/-}$ muscle fibers (Fig. 1 H, inset; Fig. 2, C and D; and Fig. S1 B). In addition, a striking and consistent feature of the *cavin-1*$^{-/-}$ muscle fibers was the presence of ruthenium red–labeled reticular structures (Fig. 1 H, insets) that resemble CAV3-positive structures in differentiating myotubes (Parton et al., 1997). Identical structures were frequently observed throughout the skeletal muscle fibers of *cavin1*$^{-/-}$ muscle (Fig. S1 A).

We further analyzed the organization of the ruthenium red–labeled WT and *cavin-1*$^{-/-}$ muscle fibers by electron tomography. In WT muscle fibers, T-tubules invariably connected to the muscle fiber surface via surface-connected caveolae (Fig. 3, A–G; and Videos 2 and 3). Surface-rendered reconstruction of the T-tubule system clearly demonstrated the connection of the T-tubule system to the surface via caveolar rosettes (Fig. 3 H). A similar 3D analysis of *cavin-1*$^{-/-}$ muscle fibers highlighted the abnormal and dilated T-tubule network within the muscle fiber as well as the surface-connected vacuoles (Fig. 3, I–L; and Video 4). In the absence of caveolae, the abnormal T-tubule network connected to the surface of the muscle fiber via the abundant vacuoles (Video 5). The reticular networks observed in thin sections throughout the *cavin-1*$^{-/-}$ muscle could be shown to be highly complex "hon-

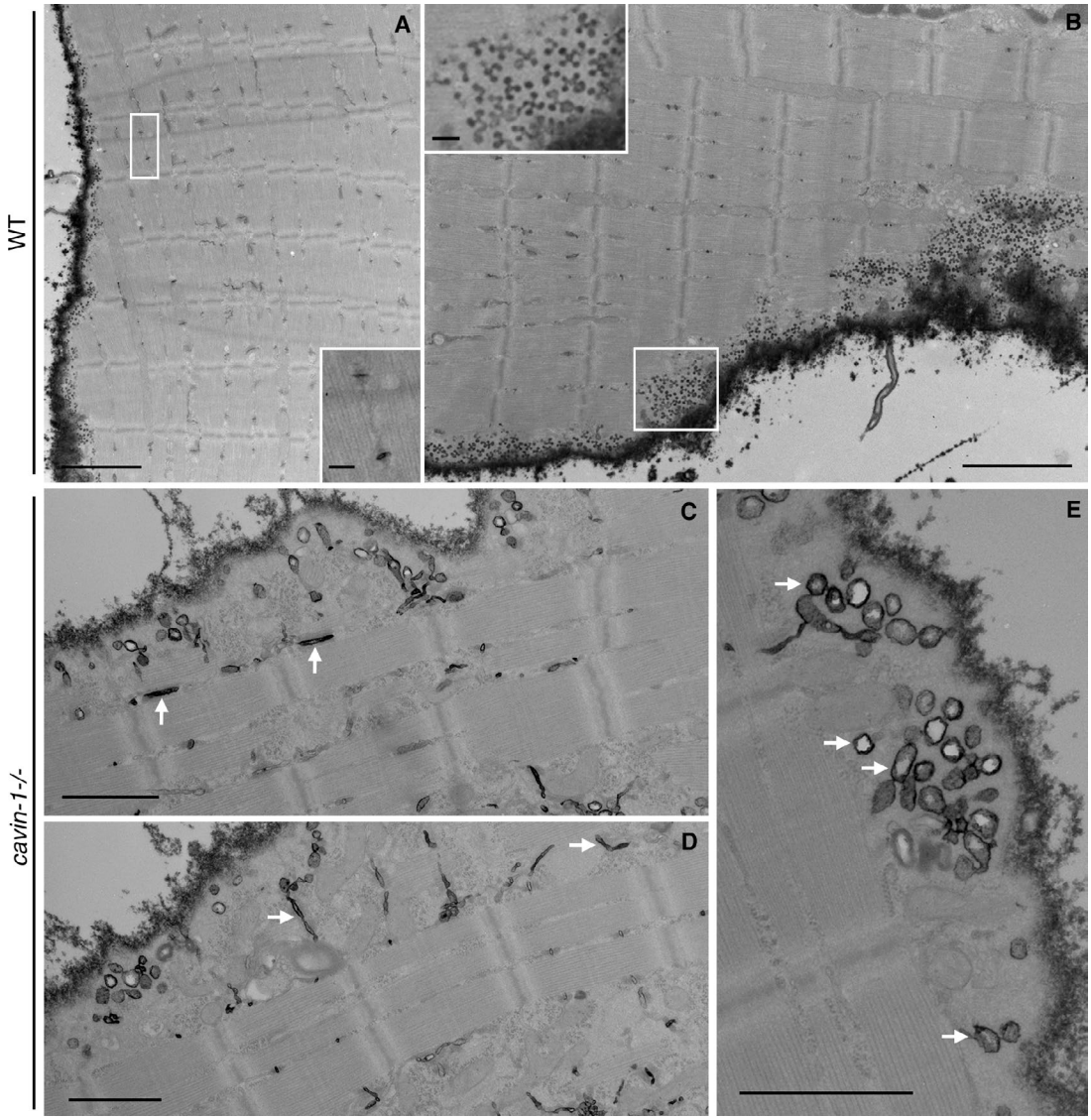

Figure 2. **Loss of Cavin-1 in muscle is associated with large vacuoles and a dilated T-tubule system.** (A and B) Ruthenium red labeling of WT muscle fibers highlighting the muscle fiber surface, T tubules (inset in A represents enlargement of boxed area) and caveolar rosettes (inset in B represents enlargement of boxed area). (C–E) Ruthenium red labeling of *cavin-1*$^{-/-}$ muscle fibers across the surface and within T tubules (arrows, C and D) and large vacuoles (arrows, E). Bars: (A and B, main images) 2 µm; (A and B, insets) 200 nm; (C–E) 1 µm.

eycomb-like" reticulated networks with multiple connections to the cell surface via large vacuoles (Fig. 3, M–O; and Fig. S3, A and B) and connections to the T-tubule network, including triad junctions (Fig. S1 A).

In view of these ultrastructural alterations in T-tubule organization, we examined the organization of several markers by light microscopy. The mechanosensitive transient receptor potential channel 1 (TRPC1), the dihydropyridine receptor (DHPR), dysferlin (Dysf), and bridging interactor 1 (Bin1; also known as Amphiphysin 2) showed relatively normal distribution by confocal microscopy but with abnormal areas of dense staining (Fig. 4 A), which likely correlate with the reticular regions observed by EM. Dysf and Bin1 expression levels were mildly elevated by Western blotting; however, we did not observe any significant differences in expression by quantitative PCR analysis (Fig. S3, C–E). This abnormal localization of T-tubule system components, together with the ultrastructural abnormalities described in this section, suggests that altered T-tubule function may in part be responsible for the RMD phenotype observed in Cavin-1–deficient patients (Rajab et al., 2010).

Cavin-4 traffics to the nucleus in the absence of Cavin-1/caveolae

In *cavin-1*$^{-/-}$ muscle, the levels of Cavin-2 and -3 and Cav1–3 were significantly reduced in comparison to WT muscle, suggesting a degree of coregulation between these proteins (Bastiani et al., 2009). However, the levels of muscle-specific Cavin-4 were unaffected by Cavin-1 deficiency; we confirmed this and the reduction in Cav3 expression by western analysis in our *cavin-1*$^{-/-}$ mice (Fig. S3, C and D).

To further explore the caveolin–cavin association, we performed immunostaining in isolated muscle fibers. In WT fibers, Cavin-4 and Cav3 strongly colocalized as a highly intricate and organized array across the muscle fiber surface, with both transverse and longitudinal structures visible (Fig. 4 B). In contrast, Cavin-1 deficiency resulted in a striking loss of Cavin-4/Cav3 ar-

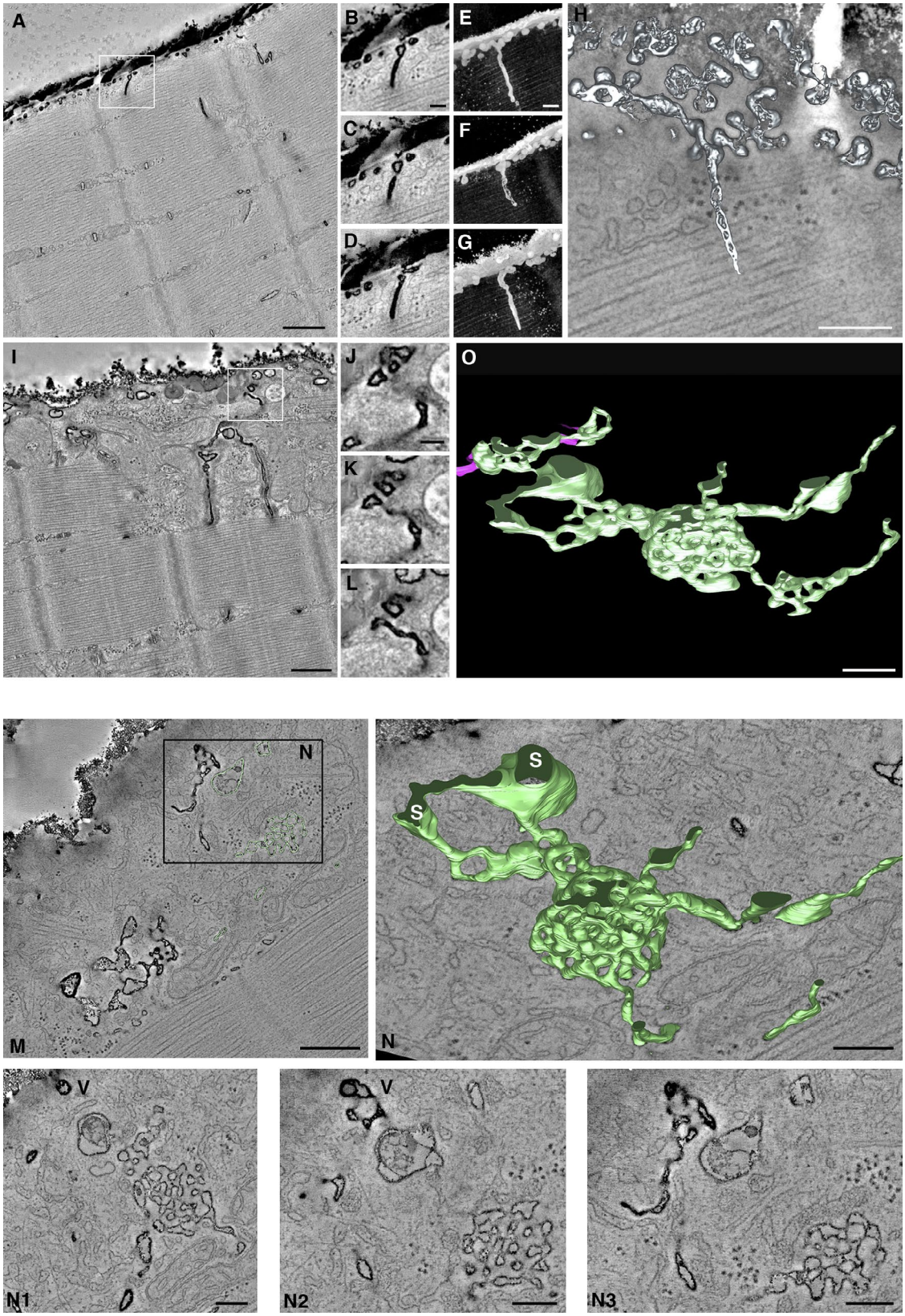

Figure 3. **Ultrastructural morphological abnormalities do not affect the relative surface area of *cavin-1*$^{-/-}$ muscle fibers.** (A–D) Single tomogram image from a ruthenium red–labeled WT muscle fiber showing T-tubule connection to the surface via caveolae (A). Tomographic slices (B–D) represent an enlargement of boxed area in A. See Video 2. (E–G) High magnification 3D images of a WT muscle fiber showing T-tubule connection to the surface via caveolae. See Video 3. (H) 3D surface-rendered reconstruction showing T-tubules connecting to the muscle fiber surface via caveolar rosettes. (I–L) Single tomogram image of a ruthenium red–labeled *cavin-1*$^{-/-}$ muscle fiber showing dilated T-tubules connecting to the surface via vacuoles (I). Tomographic slices (J–L) represent an enlargement of boxed area in I. See Videos 4 and 5. (M) Tomographic slice of a ruthenium red–labeled *cavin-1*$^{-/-}$ muscle fiber. (N) Surface-ren-

rays at the muscle fiber surface. Despite normal Cavin-4 expression levels, the intensity of Cavin-4 staining was greatly reduced at the muscle surface, consistent with a redistribution, rather than loss of Cavin-4. Dense areas of Cav3 staining were also apparent, similar to those observed with the T-tubule protein markers (Fig. 4 A) and likely corresponding to the reticular structures observed by EM (Fig. 1 H). Increasing the signal intensity of Cavin-4 staining further revealed a loss in its colocalization with Cav3 at the muscle surface (Fig. 4 B, insets), suggesting that the colocalization of Cavin-4 and Cav3 is dependent on Cavin-1. The interaction between Cavin-4 and Cav3 in muscle fibers was further defined using the Duolink proximity ligation assay (PLA), which enables the in situ identification of protein–protein interactions using secondary antibodies linked to DNA molecules (Söderberg et al., 2008). We observed a high density of fluorescent Duolink PLA signals at the surface of WT muscle fibers, indicative of an interaction between Cavin-4 and Cav3 (Fig. 4 C). Conversely, there was a significant reduction in Duolink PLA signal in *cavin-1*$^{-/-}$ muscle fibers; the level of signal was similar to that seen in the negative control. These results, in conjunction with the Cavin-4/Cav3 labeling studies, demonstrate that Cavin-1 plays an essential role in the colocalization and association of Cavin-4 and Cav3 in vivo and that a loss of Cavin-1/caveolae results in a loss of sarcolemmal organization in skeletal muscle.

Further investigation into the localization of Cavin-4 revealed that in contrast to WT muscle, Cavin-4 was predominantly localized to the nucleus of *cavin-1*$^{-/-}$ muscle fibers when cells were fixed using an alternative protocol (Fig. 4 D). In addition, Cavin-4 was shown to localize specifically to muscle nuclei in unfixed cryosections of *cavin-1*$^{-/-}$ muscle tissue (Fig. S4 A). Therefore, Cavin-4 appears to traffic to the nucleus in the absence of Cavin-1/caveolae.

Caveolar rosettes are preferentially disassembled in response to increasing membrane tension

As a model system to examine the cell-autonomous response of mature muscle fibers to changes in membrane tension in the absence of surrounding tissues and extracellular matrix, we exposed WT muscle fibers to a 15-min incubation in hypo-osmotic media, which has been previously used to study the effects of cell swelling in *mdx* muscle fibers (Wang et al., 2005). Under these conditions, muscle fibers formed numerous membrane blebs of variable size (10–80 µm in diameter). Sarcolemmal blebs were positive for Cav3 but completely negative for Cavin-1 and Cavin-4 showing a complete separation of caveolins from cavins in these regions, as confirmed using the Duolink PLA (Fig. 5, A–C).

At the ultrastructural level, hypo-osmotic treatment resulted in a significant reduction in the number of morphologically distinct sarcolemmal caveolae (overall 60% reduction in caveolar density compared with muscle fibers in iso-osmotic media) and a striking complete loss of caveolae within membrane blebs (Fig. 5, D and E). Remarkably, the remaining caveolae on the non-bleb muscle surface in hypo-osmotically treated fibers were predominantly single caveolae, with only 4% of rosettes consisting of three or more caveolae, compared with fibers in iso-osmotic media in which 39% of rosettes were associated with three or more caveolae (Fig. 5, F and G). A similar profile was observed in quantitation of caveolar rosettes from tomograms (Fig. S4 B and Videos 6 and 7) and is highlighted by 3D reconstructions of caveolar rosettes in iso-osmotic and hypo-osmotic media (Fig. 5 H). These results suggest that there is a preferential disassembly of caveolar rosettes in response to an increase in membrane tension.

Our quantitative analysis of the sarcolemmal area of *cavin-1*$^{-/-}$ muscle fibers (relative to the sarcomeric unit and excluding T-tubule membrane) was identical to WT muscle, despite the dramatically different surface architecture (Fig. 1 I). Therefore, to examine whether the organization of the membrane into caveolae and caveolar rosettes is crucial for a response to increased membrane tension, we also subjected *cavin-1*$^{-/-}$ muscle fibers to incubation in a hypo-osmotic medium and observed an increased level of cell lysis (Fig. S4, C and D; and Video 8). Therefore, these results highlight the importance of the caveolar microdomain in maintaining membrane integrity.

Re-expression of Cavin-1 rescues the null phenotype in *cavin-1*$^{-/-}$ muscle

To determine whether the previously described changes are directly caused by an absence of caveolae as a result of Cavin-1 deficiency, we examined whether Cavin1-GFP was able to rescue the null phenotype in *cavin-1*$^{-/-}$ muscle fibers. In vivo expression of Cavin1-GFP in the FDB muscle of *cavin-1*$^{-/-}$ mice was accomplished by the injection of adeno-associated virus (AAV) vectors. Western analysis of AAV-injected FDB muscle demonstrated successful expression of Cavin1-GFP, which also enhanced expression of Cav3 (Fig. 6 A and Fig. S4 E). Imaging of isolated muscle fibers revealed Cavin1-GFP localization at the muscle fiber surface; the expression of Cavin1-GFP (but not GFP reporter alone) restored the localization of both Cavin-4 and Cav3 at the muscle fiber surface (Fig. 6, B–K), as previously observed in WT muscle fibers (Fig. 4 B). Moreover, analysis of the Cavin-4–Cav3 interaction using the Duolink PLA showed a 21-fold increase in PLA signal in muscle fibers expressing Cavin1-GFP, compared with those expressing GFP reporter alone (Fig. 6, L–P).

On an ultrastructural level, expression of Cavin1-GFP (but not GFP alone), rescued caveola formation and assembly of caveolar rosettes and led to a loss of the highly convoluted membrane surface characteristic of *cavin-1*$^{-/-}$ muscle fibers (Fig. 6 Q). Finally, we investigated whether the expression of Cavin1-GFP was able to rescue the response of fibers to changes in membrane tension. Incubation of AAV-injected fibers in hypo-osmotic media for 15 min revealed that fibers expressing Cavin1-GFP showed a threefold reduction in the levels of cell lysis (mean 11.0% cell lysis in comparison to a mean 36.3% cell lysis in those expressing GFP reporter only; Fig. 6 R). Collectively, these results demonstrate that exogenous Cavin-1 is able to rescue the null phenotype in muscle

dered reconstruction highlights honeycomb structure of T tubule–connected reticulated networks as previously shown in differentiating muscle cells (Parton et al., 1997) and human *CAV3* muscle (Minetti et al., 2002). Reticulated networks are connected to the surface (S) via vacuoles (V). (N1–N3) Tomographic slices of ruthenium red–labeled *cavin-1*$^{-/-}$ muscle fiber area highlighted in N. See also Fig. S3 (A and B). (O) 3D view of surface-rendered reconstruction of area highlighted in N showing reticulated networks observed in *cavin-1*$^{-/-}$ muscle (green). Pink highlights connections to the plasma membrane. Bars: (A, I, and M) 500 nm; (B, E, and J) 100 nm; (H, N, N1–N3, and O) 200 nm.

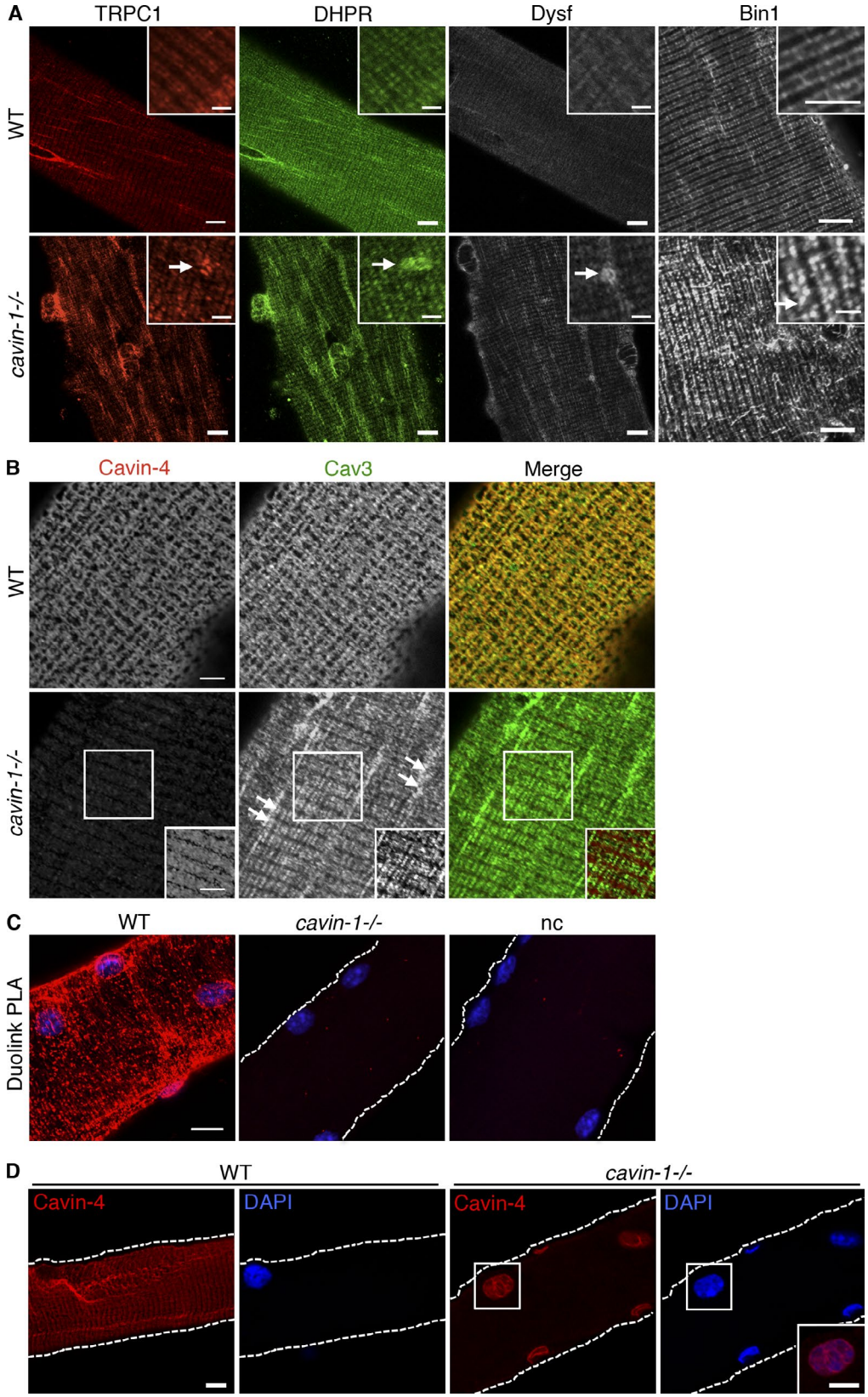

Figure 4. **Loss of Cavin-1 affects T-tubule and sarcolemmal organization in muscle.** (A) Colabeling for TRPC1 and DHPR and labeling for Dysf and Bin1 at the subsarcolemmal surface of WT and *cavin-1*$^{-/-}$ muscle fibers. (top) Insets show a typical T-tubule staining pattern for TRPC1, DHPR, Dysf, and Bin1 in WT muscle fibers. (bottom) Dense areas of staining for TRPC1, DHPR, Dysf, and Bin1 (arrows, insets) were observed within *cavin-1*$^{-/-}$ muscle fibers. Insets show a higher magnification. (B) Cavin-4/Cav3 colabeling across the surface of WT and *cavin-1*$^{-/-}$ muscle fibers. Increasing the signal intensity of Cavin-4 staining revealed that Cavin-4/Cav3 colocalization was lost in *cavin-1*$^{-/-}$ muscle fibers (insets represent boxed areas). Arrows indicate areas of dense Cav3 staining. (C) Duolink PLA in WT and *cavin-1*$^{-/-}$ muscle fibers using anti–Cavin-4 and anti-Cav3 antibodies with DAPI counterstain. Negative control

and emphasizes the importance of Cavin-1 in organizing and protecting the sarcolemmal surface of skeletal muscle fibers via the formation of caveolae.

Muscle-specific loss of Cavin-1 in an in vivo zebrafish system compromises sarcolemmal integrity

To determine the effect of Cavin-1 deficiency on in vivo muscle function, we used the zebrafish (*Danio rerio*) as a model system. We have previously shown that MO knockdown of *cavin-1b* (also known as *ptrfb*) leads to a decrease in caveolar density in the notochord of developing zebrafish embryos (Hill et al., 2008). However, there was no evidence that *cavin-1b* was expressed in zebrafish muscle. A second zebrafish *cavin-1* gene has been identified (*ptrfa*; NCBI RefSeq XM_001920667), hereafter referred to as *cavin-1a*. Cavin-1a shares 56.8% and 56.4% sequence similarity with human Cavin-1 and zebrafish Cavin-1b, respectively, and evolutionary analysis confirmed that it was placed within the Cavin-1 clade (Fig. S5, A and B). RT-PCR confirmed *cavin-1a* expression in zebrafish embryos; *cavin-1a* is maternally expressed, with an increase in expression levels around 19.5 h postfertilization (hpf; Fig. 7 A). Whole-mount in situ hybridization revealed *cavin-1a* to be a muscle-specific isoform, with strong staining within the zebrafish myotome in 48 hpf embryos (Fig. 7 B).

This apparent subfunctionalization of duplicate Cavin-1 genes in the zebrafish allowed us to examine the loss of Cavin-1 in a muscle-specific manner. To do this, we used an MO-based approach for knockdown of *cavin-1a* in WT embryos. To test the specificity of the *cavin1a*-MO, we first coinjected *cavin1a*-MO and GFP mRNA containing the MO target sequence (*cavin1a*-GFP). GFP fluorescence was abolished in embryos coinjected with *cavin1a*-MO and *cavin1a*-GFP mRNA, confirming specificity of the *cavin1a*-MO (Fig. S5 C). A dose–response curve was further generated to determine the ideal concentration for *cavin1a*-MO injections (Fig. S5 D). A loss of Cavin-1a resulted in morphants with phenotypes that fell into one of three categories: (1) normal, (2) a mild phenotype, with shorter trunks and cardiac edema, and (3) a severe phenotype with shorter, curved trunks, and cardiac edema (Fig. 7 C). MO injections are, however, known to cause off-target developmental defects, the majority of which involve the activation of p53, leading to p53-induced apoptosis (Robu et al., 2007). Therefore, we performed additional MO injections in the *tp53*^{zdf1} zebrafish line, which expresses an autosomal-dominant p53 mutation (Berghmans et al., 2005). A similar range of phenotypes was observed in *tp53*^{zdf1} *cavin1a* morphants, indicating that the phenotypes observed were not caused by off-target p53-induced apoptosis (Fig. 7 C). The ultrastructure of muscle fibers from 5-d-old embryos injected with either control or *cavin-1a* MO was examined by EM. Caveolae density was dramatically reduced in *cavin1a*-MO muscle fibers in comparison to those injected with control MO (equal to a 98.7% loss in relative caveolae density; Fig. 7, D and E). Muscle fibers from *cavin-1a* morphants further demonstrated a convoluted membrane surface, similar to that observed in *cavin-1*$^{-/-}$ mouse muscle (Fig. 1 H and Fig. S1 A) and an increased number of endosomes.

To define the functional consequences of Cavin-1a deficiency in zebrafish embryos, we investigated whether a loss of Cavin-1a resulted in compromised muscle integrity. Cavin-1a knockdown was performed in a transgenic line, *Tg(actb2:EGFP-CAAX)*^{pc10}, which expresses membrane GFP, to delineate the muscle fibers, and morphants were injected with Evans blue dye (EBD), which has previously been used to detect sites of membrane permeability in zebrafish embryos (Bassett et al., 2003; Hall et al., 2007). No evidence of EBD uptake was observed in *cavin-1a* morphants incubated in embryo media. However, incubation of 72 hpf *cavin-1a* morphants in a highly viscous medium (3% methylcellulose [MC]) followed by injection of EBD revealed uptake within muscle fibers in 17.0% of *cavin-1a* morphants (compared with only 0.8% in those injected with a control MO), indicating a loss of sarcolemmal integrity in Cavin-1a morphants in response to increased mechanical strain (Fig. 7, F and G).

Finally, we investigated whether exercise-induced membrane damage could be a common feature of muscle caveolar perturbation. To this end, we targeted a different caveolar component, Cav3, using a dominant active disease-associated mutant. We generated transgenic zebrafish lines expressing Cav3-WT-GFP or Cav3-R26Q-GFP, a mutant involved in RMD (Sotgia et al., 2003) under the Cav3 promoter (*Tg(cav3:Cav3WT-EGFP)*^{uq1rp} and *Tg(cav3:CAV3R26Q-EGFP)*^{uq2rp}, respectively). Cav3 transgene expression was confirmed by western analysis (Fig. S5 E), and in vivo imaging revealed Cav3-GFP localization at the plasma membrane of muscle fibers (Fig. 7 H) and the notochord (not depicted), consistent with a previous expression study (Nixon et al., 2005). Clutches of both Cav3WT-GFP and Cav3-R26Q-GFP showed little evidence of EBD uptake when incubated in E3, with no significant difference observed between the two zebrafish lines. However, upon incubation in 3% MC, there was a significant increase in the number of EBD-positive Cav3-R26Q-GFP embryos compared with Cav3WT-GFP embryos (31.5%, compared with 7.1% of EBD-positive Cav3WT-GFP embryos; Fig. 7, H and I). These results show that expression of a Cav3 dominant-negative mutant leads to compromised membrane integrity in zebrafish embryos, a phenotype only revealed by intense muscle activity. In conclusion, we have shown here using both MO and transgenic approaches that two caveolar components, cavins and caveolins, are essential in maintaining sarcolemmal integrity in zebrafish muscle in response to vigorous muscle activity.

Discussion

The critical role of Cavin proteins in the formation and stabilization of caveolae is now well established (Bastiani and Parton, 2010). Although the exact nature of the cavin complex association with caveolae remains unclear, recent work demonstrated that cavins may have distinct tissue-specific functions (Hansen et al., 2013), with distinct cavin subcomplexes existing within the same caveolae (Gambin et al., 2014). This study has investigated the role of the unique membrane architecture generated by Cavin-1/caveolae in skeletal muscle, providing the first

(nc) was performed on WT muscle fibers where one primary antibody was omitted. (D) Cavin-4 staining in methanol-fixed WT and *cavin-1*$^{-/-}$ muscle fibers with DAPI counterstain. Inset represents overlay of Cavin-4/DAPI labeling within nucleus in boxed areas. Muscle fibers are highlighted with dashed lines. Bars: (A) 20 µm; (B–D) 10 µm; (A, B, and D, insets) 5 µm.

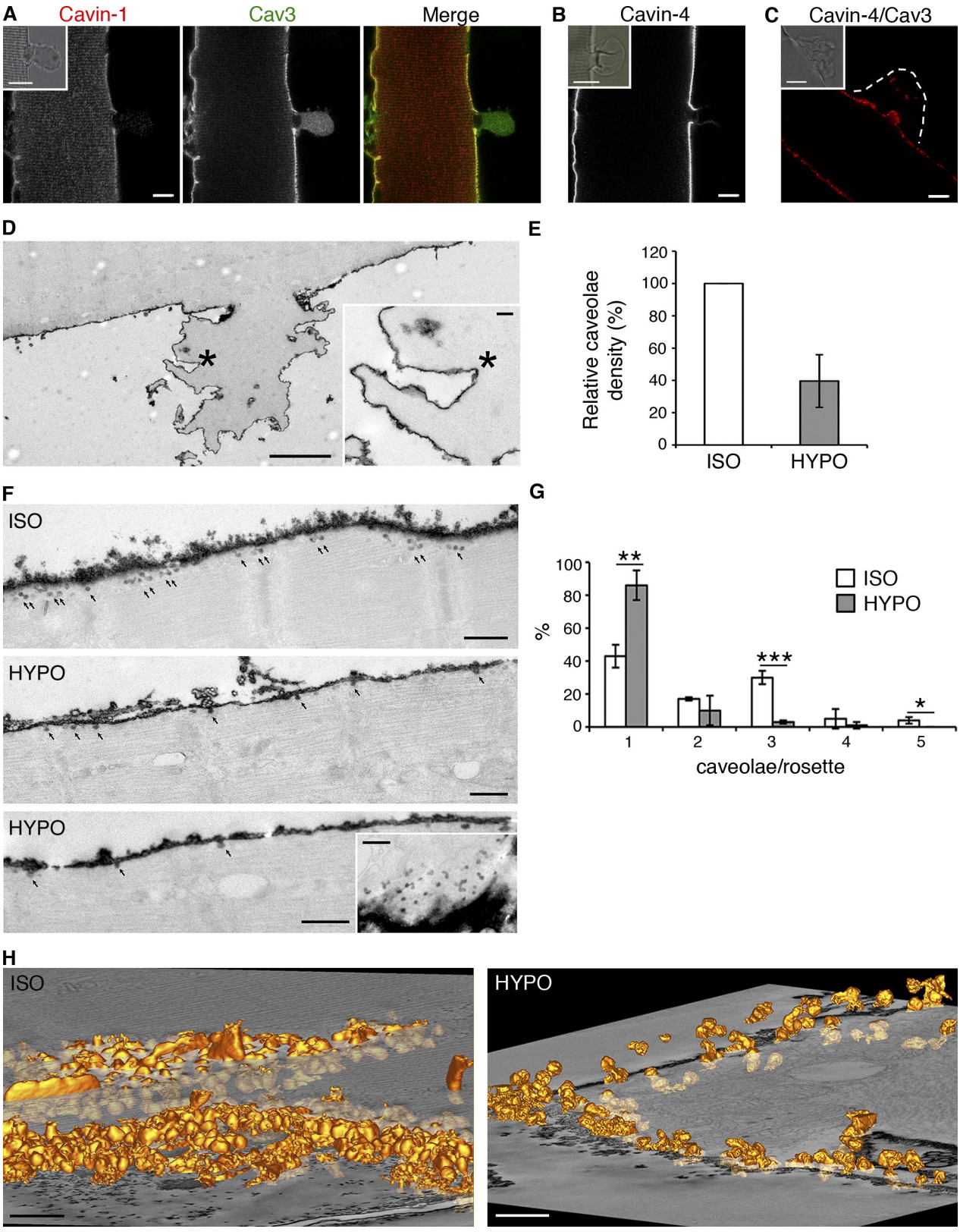

Figure 5. **Preferential disassembly of caveolar rosettes in response to increased membrane tension.** (A and B) Immunofluorescence of Cavin-1/Cav3 (A) and Cavin-4 (B) in WT muscle fibers after 15 min in hypo-osmotic (HYPO) media (insets represent brightfield image of membrane bleb). (C) Duolink PLA of Cavin-4/Cav3 interaction in WT muscle fibers after 15-min incubation in hypo-osmotic media (inset, brightfield image of membrane bleb). Dashes outline the membrane bleb. (D) EM analysis of a ruthenium red–labeled WT muscle fiber after 15 min in hypo-osmotic media (inset, higher magnification of bleb area indicated by asterisks). (E) Relative caveolae density of WT fibers in hypo-osmotic media was 39.6 ± 16.3% (means ± SD; compared with WT fibers incubated in iso-osmotic [ISO] media). (F) Ruthenium red–labeled WT muscle fibers in iso-osmotic or hypo-osmotic media. Arrows indicate caveolae beneath the sarcolemma. Several single caveolae are observed in hypo-osmotic–treated muscle fibers (inset). (G) Quantitation of number of caveolae

detailed characterization of the skeletal muscle phenotype of *cavin-1*$^{-/-}$ mice. We have used several experimental approaches using mammalian muscle samples, isolated muscle fibers, and zebrafish models to gain fundamental insights into the role of muscle caveolae. Our findings suggest that caveolae play an essential role in mechanoprotection in skeletal muscle.

An early morphological study characterized the effect of myofiber lengthening on caveolae flattening, albeit under extreme nonphysiological levels of stretching, questioning a general role for caveolae in providing membrane for sarcolemmal changes (Dulhunty and Franzini-Armstrong, 1975). More recent studies demonstrate a physiological role for caveolae in limiting membrane tension in response to cell stretch or swelling (Kozera et al., 2009; Sinha et al., 2011). However, skeletal muscle studies relied on cultured myotubes, which lack the structural and functional characteristics of differentiated mature skeletal muscle. Therefore, we have used mature mouse muscle fibers to provide further insights into the role of caveolae as a mechanoprotective component of skeletal muscle. In WT muscle fibers, the striking rosette organization of caveolae, in which few caveolae are directly connected to the sarcolemma but indirectly via a neck common to 3–5 caveolae, was a consistent feature over the entire muscle fiber surface. These enigmatic structures are a characteristic feature of differentiating muscle cells, although their cellular role has remained unknown (Parton et al., 1997). Our findings suggest that caveolar rosettes may be preferentially sensitive to membrane force, allowing rapid disassembly of a single unit containing multiple caveolae into the bulk membrane, providing a mechanism for larger scale reorganization of the membrane. The detailed characterization of the proposed mechanism for flattening of a group of caveolae, rather than a single caveolae, is amenable to modeling and biophysical analysis, but these results provide a testable model for the function of this characteristic caveolar feature.

We demonstrate here that caveolae link the T-tubules to the muscle fiber surface, supporting earlier serial section analysis (Rayns et al., 1968). A genetic loss of Cavin-1/caveolae resulted in significant disruptions to the sarcolemmal and T-tubule system in muscle. The aberrant T-tubule formation observed here and in Cav3-deficient muscle resembles immature muscle cells, where there is a larger proportion of longitudinal tubules in addition to transverse tubules (Minetti et al., 2002) and very characteristic Cav3-positive membrane networks (Parton et al., 1997). These abnormalities likely lead to the abnormal action potential propagation observed in these muscle fibers and may underlie the rippling muscle phenomenon seen in patients (Lamb, 2005). Despite these morphological differences, however, the T-tubule system was still able to connect to the muscle fiber surface via abnormal vacuoles; although it remains unclear how this occurs and what effect it would have on T-tubule function, it suggests the importance of a distinct microdomain in connecting the T-tubule to the muscle surface. An intriguing possibility is that caveolar flattening during normal muscle contraction functions to not only maintain the integrity of the sarcolemma but that caveolar clusters at the neck of the T-tubules could be particularly important in buffering any forces at the neck of the T-tubules as the fiber changes diameter.

The increased susceptibility to osmotic stress and impaired membrane integrity displayed by caveola-deficient *cavin-1*$^{-/-}$ muscle fibers, without any apparent change in total surface area, highlights the essential role of the caveolae structure in mediating a response to changes in membrane tension. The reformation of caveolae and caveolar rosette structures upon recapitulation of Cavin-1 expression further emphasizes the importance of Cavin-1 in caveolar biogenesis. The loss of Cavin-1 and Cavin-4 from membrane blebs in response to increased membrane tension also underscores an important mechanosensory role for the cavins. In this respect, the finding that Cavin-4 associates with the nuclei of *cavin-1*$^{-/-}$ muscle fibers is particularly intriguing as it raises the possibility that under physiological conditions, Cavin-4 may be released from the caveolae and shuttle to the nucleus. In this model, the flattening of caveolae in response to membrane stress or stretch allows the release of cavins to signal further into the cell (Sinha et al., 2011; Parton and del Pozo, 2013). An intriguing hypothesis, which can now be tested, is that localized flattening of individual caveolae in response to membrane stress could release the cavin complex over time as a signal for specific pathways, including muscle hypertrophy. The role of the muscle cavin complex in this process awaits further dissection.

The isolation of muscle fibers and hypo-osmotic treatment used here, are clearly nonphysiological manipulations that allowed an analysis of muscle fiber properties in the absence of the usual extracellular matrix environment crucial for muscle function. Nonetheless, we identified dramatic differences in cell-autonomous muscle fiber properties using these systems, which could be partially compensated in vivo by the extracellular environment. However, the apparent subfunctionalization of duplicated Cavin-1 genes into muscle and nonmuscle domains in the zebrafish enabled the muscle-specific knockdown of Cavin-1 within a physiological setting. An absence of Cavin-1 in muscle caused a dramatic reduction in caveolae density in zebrafish embryos. Furthermore, a loss of Cavin-1a and expression of a Cav3 dystrophy mutant leads to reduced sarcolemmal integrity in zebrafish embryos in response to increased mechanical strain. However, the EBD-positive muscle fibers observed in both *cavin-1a* knockdown and Cav3-R26Q-GFP embryos were still intact and did not display evidence of failed fiber attachment as shown previously in the dystrophin and laminin-α2–null zebrafish models (Bassett et al., 2003; Hall et al., 2007). Therefore, the loss of membrane integrity observed here occurs via a mechanism that is dissimilar to these previously described muscular dystrophy models. Our findings are consistent with a mechanism whereby modulating cavin/caveolin levels in muscle leads to small lesions in the membrane, which would weaken the sarcolemma and eventually lead to apoptosis. Collectively, our data suggest that an increase in membrane fragility contributes to the disease phenotype in caveola-related

associated with caveolar rosettes (caveolae/rosette) after incubation in iso-osmotic or hypo-osmotic media: 43 ± 7%, 17 ± 1%, 30 ± 4%, 5 ± 6%, and 4 ± 2% of caveolae from muscle fibers in iso-osmotic media had 1–5 caveolar rosettes, respectively; 86 ± 9%, 10 ± 9%, 3 ± 1%, 1 ± 2%, and 0 ± 0% of caveolae from muscle fibers in hypo-osmotic media had 1–5 caveolar rosettes, respectively. Error bars show means ± SD. Quantitation was performed on >440 caveolae from three different muscle fibers for both iso-osmotic and hypo-osmotic treatments. (H) 3D view of surface-rendered reconstructions of caveolar rosettes (yellow) in WT fibers incubated in iso-osmotic or hypo-osmotic media. See Videos 6 and 7. Bars: (A–C) 10 µm; (D and F) 2.5 µm; (D [inset] and H) 200 nm. *, $P \leq 0.05$; **, $P \leq 0.01$; ***, $P \leq 0.001$.

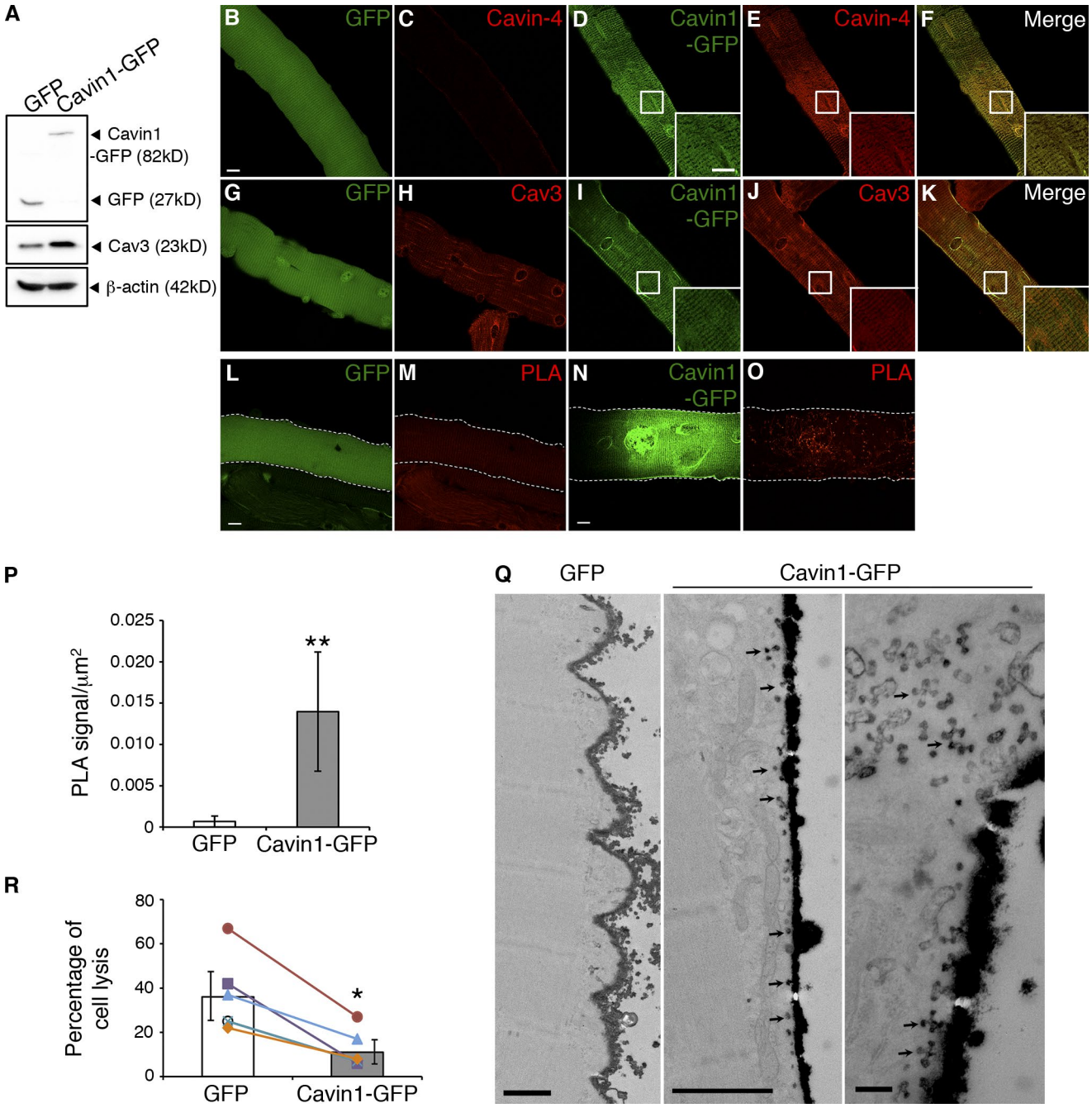

Figure 6. **Exogenous Cavin1-GFP expression in *cavin-1*$^{-/-}$ muscle fibers rescues the null phenotype.** (A) Western analysis of *cavin-1*$^{-/-}$ muscle fibers expressing GFP reporter or Cavin1-GFP using anti-GFP and anti-Cav3 antibodies. β-Actin demonstrates protein loading; 50 µg protein lysate was loaded. (B–K) Cavin-4 (B–F) and Cav3 (G–K) immunostaining in *cavin-1*$^{-/-}$ muscle fibers expressing GFP reporter (B and G) or Cavin1-GFP (D and I). Insets represent enlargement of boxed areas. (L–O) Duolink PLA using anti–Cavin-4 and anti-Cav3 antibodies in *cavin-1*$^{-/-}$ muscle fibers expressing GFP reporter (L) or Cavin1-GFP (N). Muscle fibers are highlighted with dashed lines. (P) PLA signal in *cavin-1*$^{-/-}$ muscle fibers was 0.0007 ± 0.0007 dots/µm^2 and 0.014 ± 0.007 dots/µm^2 in fibers expressing GFP reporter or Cavin1-GFP, respectively. Quantitation performed on 15 GFP reporter and 9 Cavin1-GFP–expressing muscle fibers from AAV injections of two *cavin-1*$^{-/-}$ mice. (Q) Ruthenium red–labeled muscle fibers expressing GFP reporter or Cavin1-GFP. Arrows indicate single caveolae (middle) and rosettes (right). (R) Mean percentage of cell lysis was 36.3 ± 6.9% and 11.0 ± 3.4% in *cavin-1*$^{-/-}$ muscle fibers expressing GFP reporter or Cavin1-GFP, respectively, and is represented as a column graph. Quantitation was performed on 85 and 99 muscle fibers expressing GFP reporter or Cavin1-GFP, respectively, from six *cavin-1*$^{-/-}$ mice. Dot plots represent percentage of cell lysis observed for individual mice; note that the percentage of cell lysis is consistently higher in the absence of Cavin-1. Error bars are means ± SEM. *, $P \leq 0.05$; **, $P \leq 0.01$. Bars: (B–O) 10 µm; (Q, left and middle images) 1 µm; (Q, right image) 200 nm.

muscle disease, which affects pathways distinct to those involving Cavin-1/caveolae in metabolism and lipodystrophy (Liu et al., 2008a). In support of this, we have previously hypothesized that adipose tissue explants lacking Cav1 are intrinsically more fragile, suggesting a general loss of protection from caveolae, independently of changes in adipose tissue metabolism (Martin et al., 2012; Parton and del Pozo, 2013). However, additional evidence suggests that Cavin-1 may recruit the membrane re-

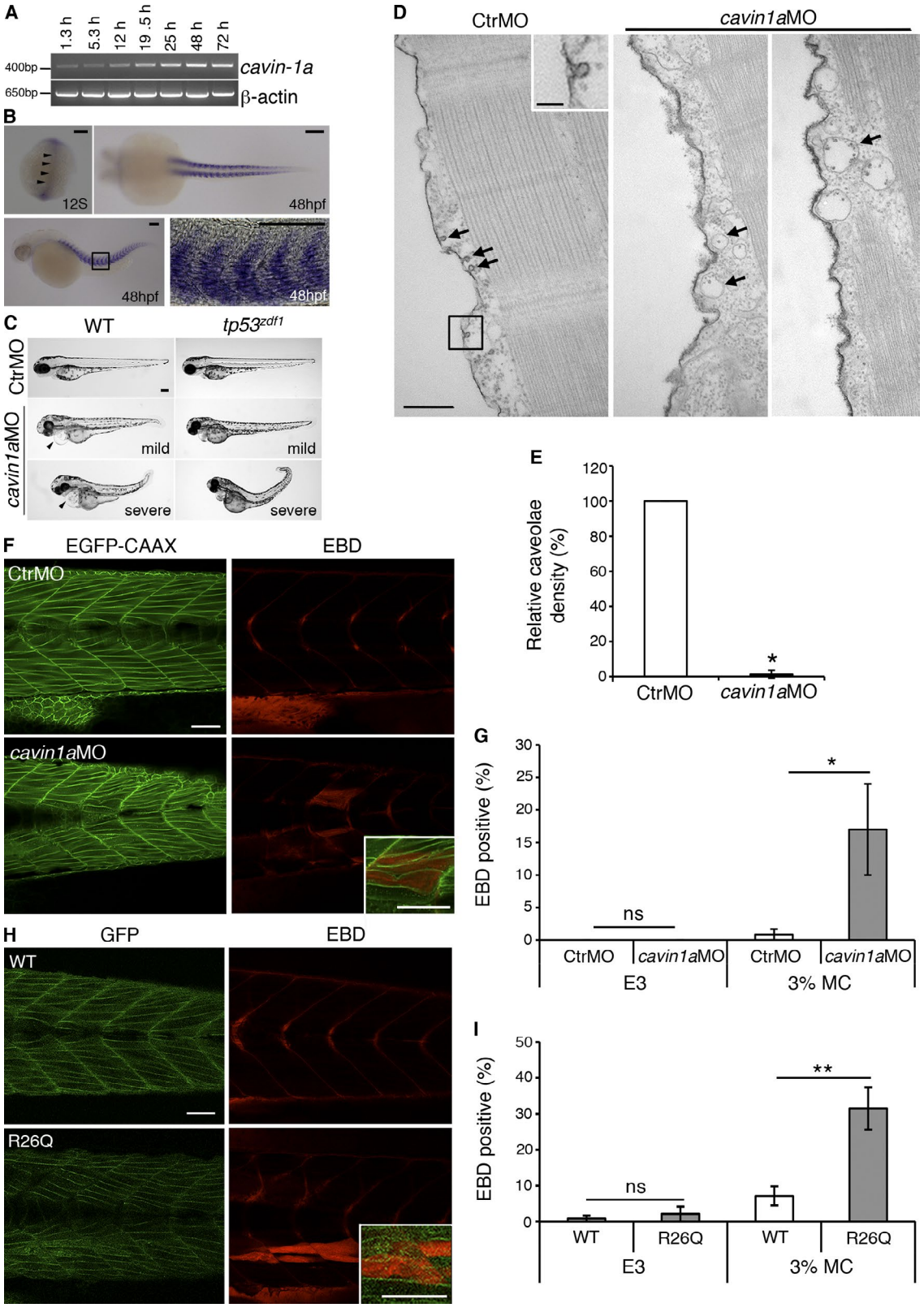

Figure 7. **Caveolae are essential for maintaining muscle integrity in the zebrafish.** (A) Temporal expression of *cavin-1a* mRNA in 1.3–72-hpf zebrafish embryos. (B) Expression pattern of *cavin-1a* in zebrafish embryos using whole-mount mRNA in situ hybridization. Dorsal view of a 12-somite (12S) embryo shows faint labeling for *cavin-1a* (arrowheads). At 48 hpf, *cavin-1a* expression is observed exclusively within the zebrafish myotomes, shown here in dorsal (top right) and lateral (bottom left) view; anterior to left in both images. Note the lack of notochord labeling in the dorsal view. Image in bottom right represents magnification of boxed area. (C) WT and *tp53*^{zdf1} zebrafish embryos were injected with control or *cavin1a* MO (CtrMO and *cavin1a*MO, respectively) and abnormal morphants (classified as mild or severe) imaged at 72 hpf. Arrowheads indicate cardiac edema. (D) Ruthenium red–labeled isolated muscle fibers from control MO and *cavin1a*MO embryos. Arrows indicate caveolae (left image) or endosomes (middle and right images). Inset

pair protein MG53 to sites of damage (Zhu et al., 2011) in a process that also involves dysferlin and caveolin-3 (Cai et al., 2009) and that internalization of membrane lesions is mediated in a caveolar-dependent manner (Corrotte et al., 2013). Therefore, it remains possible that caveolae may nonetheless be involved in membrane repair pathways in skeletal muscle.

In conclusion, we have used mouse and in vivo zebrafish models to provide fundamental new insights into the pathogenesis of caveola-related muscle disease, suggesting that caveolae are an essential feature for mechanoprotection in skeletal muscle. Determining the etiology of caveola-related muscle disease will be crucial for understanding caveola biogenesis and function in muscle and for the development of therapeutic strategies in human patients.

Materials and methods

Animal experiments

Cavin-1$^{-/-}$ mice, generated by replacing part of Exon 1 of the *cavin-1* gene with a LacZ/Neo fusion cassette, were obtained from Boston University School of Medicine (Liu et al., 2008a). *Cavin-1*$^{-/-}$ mice, WT controls (both backcrossed onto the same C57BL/6 strain for 10 generations), and adult zebrafish were fed and maintained according to institutional guidelines (University of Queensland). Zebrafish embryos were obtained from natural spawnings of zebrafish and raised at 28.5°C in standard E3 (5 mM NaCl, 0.17 mM KCl, 0.33 mM $CaCl_2$, and 0.33 mM $MgSO_4$). All animal experiments were approved by the University of Queensland Animal Ethics Committee.

Antibodies and reagents

Antibodies were obtained from the following sources: mouse anti-Cav3 and mouse anti–Pecam-1 from BD, rabbit anti-TRPC1 from Alomone Labs, mouse anti-DHPR (MAB 427) from EMD Millipore, rabbit anti-PTRF from Sigma-Aldrich, mouse anti-actin (clone C4) from EMD Millipore, mouse anti-dysferlin (NCL-Hamlet) from Leica, mouse anti-bin1 (clone 99D) from Merck, mouse anti-MHC (F59) from Developmental Studies Hybridoma Bank, and mouse anti-GFP from Roche. Anti–mouse or anti–rabbit Alexa Fluor 488– and 555–conjugated secondary antibodies were obtained from Life Technologies. Affinity-purified rabbit polyclonal antibodies against Cavin-4 (peptide sequence Ac-CGDDESLLLELKQSS) and Cavin-1 (Ac-CTEESDAVLVDKSDSD) were raised using keyhole limpet hemocyanin–conjugated peptides as described previously (Bastiani et al., 2009). All other reagents were from Sigma-Aldrich unless otherwise specified.

Histology

Quadriceps muscles from 3–5-mo-old WT and *cavin-1*$^{-/-}$ mice were fixed in 4% PFA and embedded in paraffin for sectioning. Routine hematoxylin and eosin staining was performed on paraffin sections by the Queensland Institute of Medical Research (QIMR) Berghofer Medical Research Institute histology service. Digital images were captured at RT under bright-field illumination using DP Capture software (Olympus) on a microscope (BX-51; Olympus; 20×/0.75 NA Plan Apochromat differential interference contrast [DIC] objective) with a color camera (DP-71 12 Mp; Olympus) and raw images assembled using Photoshop (Adobe).

Hanging test and treadmill experiments

The four-limb hang tests were performed as previously described (Deacon, 2013) and based on the Treat-NMD recommended protocol for "The use of four-limb hanging tests to monitor muscle strength and condition over time" (Carlson, 2011). In brief, mice were placed on a 43 × 43–cm wire mesh screen, which was slowly inverted over 2 s. Total time (minutes) mouse was able to grip the screen was recorded. Mice were subjected to forced treadmill running protocols as previously described (Pearen et al., 2012), with minor changes. In brief, mice were run on an Exer 3/6 Treadmill (Columbus Instruments) with mild electrical stimulus at 10% inclination. Mice were initially trained by running once per day for 30 min at 10 m/min for 3 d. To determine maximum running speed, mice were acclimatized for 30 min at 10 m/min followed by acceleration for 1 m/min until exhausted. To determine endurance, mice were acclimatized for 60 min at 10 m/min followed by incremental acceleration (1 m/min every 5 min) to a maximum speed of 20 m/min until exhaustion. Exhaustion was defined by an inability to run for >10 s.

Muscle fiber isolation

Muscle fibers were isolated from the FDB of age- and gender-matched adult mice as described previously (Rahkila et al., 1996). In brief, FDB muscle was incubated in 700 U/ml Worthington's type II collagenase in dissociation medium (DMEM supplemented with 2 mM L-glutamine, 100 U/ml penicillin, and 100 µg/ml streptomycin), and fibers were resuspended in growth media (dissociation media supplemented with 10% fetal bovine serum). Fiber suspensions were spread onto 3-cm Matrigel-coated (BD) cell culture dishes and allowed to adhere for 2 h or overnight (16 h) at 37°C (the same results were observed regardless of 2- or 16-h adherence times).

Immunostaining

Immunofluorescence of muscle fibers was performed as previously described with minor changes (Rahkila et al., 1996). In brief, fibers were fixed overnight in 4% PFA and permeabilized with 0.5% Triton X-100, or fixed in ice-cold methanol for 1 min. Fibers were blocked in 0.2% fish skin gelatin/0.2% BSA andincubated overnight at 4°C in primary antibodies (diluted in blocking solution) followed by incubation in secondary antibodies at RT for 1 h. Nuclear counterstain with DAPI (Sigma-Aldrich) was performed where indicated, and fibers were mounted in Mowiol (EMD Millipore). Confocal images were captured at RT using ZEN software on an upright confocal microscope (LSM

represents boxed area. (E) Relative caveolae density of muscle fibers from *cavin1a*MO embryos was 1.4 ± 2.0% (means ± SD), compared with muscle fibers from control MO embryos. Quantitation performed on four control MO and six *cavin1a* MO muscle fibers. (F) EBD uptake in 96 hpf *Tg(actb2:EGFP-CAAX)*^{pc10} embryos expressing EGFP-CAAX injected with control MO or *cavin1a* MO and incubated in 3% MC. Inset shows higher magnification of EGFP-CAAX/EBD-positive muscle fibers. (G) 0.0 ± 0.0% of control MO and *cavin1a*MO embryos were EBD positive after incubation in E3 (means ± SEM; 28 control MO and 47 *cavin1a* MO embryos from three separate microinjections). 0.8 ± 0.8% of control MO and 17.0 ± 7.0% of *cavin1a* MO embryos were EBD positive after incubation in 3% MC (means ± SEM; 105 control MO and 111 *cavin1a* MO embryos from eight separate microinjections). (H) EBD uptake in 96 hpf embryos expressing Cav3-WT-GFP (WT) or Cav3-R26Q-GFP (R26Q) after incubation in 3% MC. Inset shows higher magnification of GFP/EBD-positive muscle fibers. (I) 0.8 ± 0.8% of WT and 2.1 ± 2.1% R26Q embryos were EBD positive after incubation in E3 (means ± SEM; 71 WT and 33 R26Q embryos from five and four clutches, respectively). 7.1 ± 2.6% of WT and 31.5 ± 5.9% R26Q embryos were EBD positive after incubation in 3% MC (130 WT and 126 R26Q embryos from seven and six clutches, respectively). Uptake was performed in two separate founder lines for both WT and R26Q to ensure that phenotypes observed were not caused by Tol2 integration sites. *, $P \leq 0.05$; **, $P \leq 0.01$. ns, not significant. Bars: (B and C) 200 µm; (D, main images) 1 µm; (D, inset) 200 nm; (F and H, main images and insets) 50 µm.

510; Carl Zeiss; Plan Apochromatic 63×/1.4 NA oil DIC objective) using the predefined ZEN software configurations for Alexa Fluor 555, Alexa Fluor 488, DAPI, and EGFP. Bright-field images were captured at RT using DP Capture software on a microscope (BX-51; Plan Apochromat 60×/1.35 NA oil DIC objective) with a color camera (DP-71 12 Mp). Raw images were assembled using Photoshop (Adobe). For muscle cryosections, gastrocnemius mouse muscle was snap frozen in isopentane-cooled liquid N_2 and 8-µm-thick cryosections obtained using a Leica microtome. Cryosections were then blocked in 0.2% fish skin gelatin/0.2% BSA; immunostaining and confocal imaging were performed as described in this section for isolated muscle fibers.

EM

Ruthenium red labeling of muscle fibers was performed as described previously (Parton et al., 2002). Electron tomography and segmentation was performed using methods described previously (Kremer et al., 1996; Mastronarde, 2005; Richter et al., 2008). In brief, 300-nm-thick sections were cut using an ultramicrotome (EM UC6; Leica). Dual-axis tilt series data were collected on an field-emission gun–transmission electron microscope (Tecnai F30; FEI Company) operating at 300 kV, over a tilt range of ±66° at 1.5° increments, using SerialEM software (The Boulder Lab for 3D Electron Microscopy). Tilt series were reconstructed with the R-weighted back projection algorithm using IMOD/Etomo software (The Boulder Lab for 3D Electron Microscopy) and segmented using IMOD's automated isosurface rendering function. The fraction of the sarcolemmal surface occupied by caveolae or other sarcolemmal vesicular elements was estimated by intersection counting of ruthenium red–labeled sarcolemma using standard stereological methods, as described previously (Parton, 1994). Note that as a result of overprojection effects, the relative contribution of the caveolae or other surface-connected structures to the total surface area can be overestimated, as described previously (Weibel, 1979; Griffiths et al., 1989). The error will be greater for smaller structures/thicker sections. Using a section thickness of 60 nm and assuming a caveolar or sarcolemmal vesicle diameter of 57 and 115 nm, respectively (Fig. S2 A), correction factors of 0.43 and 0.60 can be applied to the percent contribution of caveolae and *cavin1*$^{-/-}$ sarcolemmal vesicles to the total surface area (Weibel, 1979). These correction factors are approximates only and give an estimate of possible error. To gain an independent estimate of surface area occupied by caveolae, the surface area of individual caveolar rosettes, including interconnecting tubular elements, was measured after surface rendering of tomograms in three dimensions (assuming a section collapse factor of 1.4× as in previous studies; Richter et al., 2008). These measurements, combined with measurements of caveolar density in 1-µm^2 regions of the sarcolemma, revealed that caveolae can contribute ≤56% of the sarcolemmal surface area. T tubules were not included in these analyses. The honeycomb-like structure was manually rendered with IMOD software using the Drawing tools and Interpolator (Noske et al., 2008). Isosurface (threshold) rendering was performed with IMOD software. For adult muscle sections, gastrocnemius muscle was dissected from 4-mo-old WT and *cavin-1*$^{-/-}$ mice and processed for EM using a modification of the method of Nguyen et al. (2011). In brief, muscle was rapidly excised, immersed in a solution of 2.5% glutaraldehyde in PBS, and immediately irradiated in a Pelco Biowave (Ted Pella, Inc.) for 3 min at 80 W under vacuum. Samples were transferred to a fresh solution of 2.5% glutaraldehyde in PBS and left for 30 min at RT before washing in 0.1 M cacodylate buffer. Samples were then immersed in a solution containing potassium ferrocyanide (3%) and osmium tetroxide (2%) in 0.1 M cacodylate buffer for 30 min at RT and then in a filtered solution containing thiocarbohydrazide (1%) for 30 min at RT, osmium tetroxide (2%) for 30 min, and then in 1% aqueous uranyl acetate for 30 min at 4°C. After a further staining step of 20 min in 0.06% lead nitrate in aspartic acid, pH 5.5, at 60°C, samples were dehydrated and embedded in Epon LX112 resin.

Western blotting

Tissue lysates from WT and *cavin-1*$^{-/-}$ skeletal muscle and zebrafish embryos were prepared as described previously (Bastiani et al., 2009). In brief, samples were homogenized using a T10 basic Ultra-Turrax homogenizer (IKA) in ice-cold radioimmunoprecipitation assay buffer (50 mM Tris-HCl, pH 8.0, 150 mM NaCl, 1% NP-40, 0.5% sodium deoxycholate, and 0.2% sodium dodecyl sulfate) containing cOmplete protease inhibitors (Roche) and immediately supplemented with 4× Laemmli's sample buffer (240 mM Tris-HCl, pH 6.8, 40% glycerol, 8% sodium dodecyl sulfate, and 0.04% bromophenol blue) and 10 mM DTT. Protein concentrations were determined using the bicinchoninic acid protein assay kit (Thermo Fisher Scientific). Protein samples were analyzed by Western blotting and detected using the ChemiDoc MP system (Bio-Rad Laboratories) as per the manufacturer's instructions. Band intensities were quantified using ImageJ (National Institutes of Health).

Quantitative RT-PCR

Total RNA was isolated using TRIzol reagent (Life Technologies), treated with Turbo DNase I (Life Technologies) and RNA purified using the RNeasy mini kit (QIAGEN), all according to the manufacturer's instructions. 1 µg of total RNA was reverse transcribed with oligo(dT)12–18 primers using the SuperScript III First-Strand Synthesis System for RT-PCR (Life Technologies). Quantitative PCR was performed in duplicate for four independent cDNA preparations using the TaqMan Universal Master Mix (Life Technologies) on a real-time PCR system (ViiA7; Applied Biosystems). Gene expression data were analyzed using the ΔΔCt method. TaqMan Gene Expression Assay PCR primers were purchased from Life Technologies: Mm00489257_m1 (*DHPR/CACNA1S*), Mm00441975_m1 (*TRPC1*), Mm00458050_m1 (*DYSF*), Mm00437457_m1 (*BIN1*), and Mm00446968_m1 (*HPRT1*).

Duolink in situ PLA

Muscle fibers were fixed overnight in 4% PFA and incubated in primary antibodies (anti-Cavin-4 and anti-Cav3) as per the immunostaining protocol. Anti–mouse PLUS and anti–rabbit MINUS PLA probes were used as secondary antibodies. Ligation, amplification, and detection steps (using the Orange detection kit) were performed according to the manufacturer's instructions (Olink Bioscience) followed by counterstaining with DAPI where indicated. Confocal images were captured and analyzed as per the immunostaining protocol. Muscle fiber area was calculated using the measurement tool in ImageJ, and PLA signals were counted using the count tool in Photoshop.

Hypo-osmotic stress experiments

Muscle fibers were cultured in growth media overnight at 37°C. Fibers were incubated in iso-osmotic media (growth media) or hypo-osmotic solution (made by reducing NaCl concentration to 30% by diluting growth media with a solution containing 1.8 mM $CaCl_2$, 0.814 mM $MgSO_4$, and 5.33 mM KCl) for 15 min at RT. Time-lapse images were captured at RT on a microscope (EVOSfl; Advanced Microscopy Group) using an UPlan Fluor N 4×/0.13 NA PhP objective (Olympus) under phase contrast.

AAV transduction of muscle

Full-length mouse *cavin-1* cDNA containing a C-terminal GFP tag was cloned into pENTR1A and recombined into a pAAV-multiple cloning site vector using the Gateway system (Life Technologies). Recombinant adeno-associated virus (rAAV2/1) vectors were generated

(P. Koebel, Institut de Génétique et de Biologie Moléculaire et Cellulaire, Illkirch, France) as previously described (Cowling et al., 2011) via triple transfection of an AAV-293 cell line with pAAV insert containing the insert under the control of the cytomegalovirus promoter and flanked by serotype 2 inverted terminal repeats, pXR1 containing replication and capsid genes of AAV serotype 1, and pHelper encoding the adenovirus helper functions. AAV particles were released from cells using three freeze/thaw cycles followed by incubation in 50 U/ml Benzonase at 37°C for 30 min and cleared by centrifugation. Viral vectors were purified using Iodixanol gradient ultracentrifugation followed by dialysis and concentration against Dulbecco's PBS and quantified by real-time PCR using a plasmid standard pAAV-EGFP. Titers are expressed as viral genomes per milliliter, and rAAV titers used here were 5–7 × 10^{11} viral genomes/ml. 2–3-mo-old WT and *cavin-1*$^{-/-}$ mice were placed under isoflurane; FDB muscles were injected with 20 µl Cavin1-GFP-AAV2/1 (right foot) or GFP-AAV2/1 (left foot) preparations. After 4 wk, mice were sacrificed by CO_2 asphyxiation, and muscle fibers were isolated from FDB as per the muscle fiber isolation protocol.

RT-PCR

To amplify *D. rerio cavin-1a*, the following primers were used: *cavin-1a* forward, 5′-TCTCAAGCGGAAGAACATCA-3′, and *cavin-1a* reverse, 5′-GTTCCGAACTTCCCCATCTT-3′. Amplification of β-actin was performed using primers as described previously (Hill et al., 2008). Total RNA was isolated from zebrafish embryos using a total RNA isolation kit (QIAGEN). cDNA was transcribed using reverse transcription (SuperScript III; Invitrogen), and amplification was performed as described previously (Hill et al., 2008). All primers used were from Integrated DNA Technologies.

Whole-mount in situ hybridization

Cavin-1a was subcloned into pGEM-T Easy from an IMAGE clone (ID 7234921) purchased from Millennium Science. The *cavin-1a* probe was synthesized by in vitro transcription using SP6 polymerase and DIG RNA labeling mix (Roche). Zebrafish embryos were removed from their chorions, fixed in 4% PFA, and stored at −20°C in methanol until required. In situ hybridization was performed as described previously with minor modifications (Thisse et al., 1993). In brief, embryos were rehydrated back into 100% PBST (PBS/0.1% Tween 20). Embryos older than 24 hpf were incubated in 10 µg/ml Proteinase K for 10 min. Embryos were postfixed in 4% PFA for 20 min and rinsed 2 × 5 min in PBST. Prehybridization was performed at 65°C for 1 h in hybridization buffer (HYB; 50% formamide, 5× SSC, 50 µg/ml heparin, 500 µg/ml tRNA, 0.1% Tween 20, and 9 mM citrate). Embryos were incubated in *cavin-1a* probe in HYB overnight at 65°C. Embryos were washed at 65°C for 10 min in 70% HYB/30% 2× SSC, 10 min in 30% HYB/70% 2× SSC, 10 min in 2× SSC, 2 × 15 min in 0.2× SSC, and 2 × 15 min in 0.05× SSC. Further washing was performed at RT for 5 min in 70% 0.05× SSC/30% PBST, 5 min in 30% 0.2× SSC/70% PBST, and 5 min in PBST followed by blocking for 1 h in PBST with 2% BSA and 2% horse serum. Embryos were incubated overnight at 4°C with preabsorbed alkaline phosphatase–coupled anti-digoxigenin antibody (Roche) diluted in blocking solution. Embryos were washed 6 × 15 min in PBST at RT and developed in nitro blue tetrazolium/5-bromo-4-chloro-3-indolyl-phosphate (NBT/BCIP) solution (Roche). Reaction was stopped in PBST, and embryos were refixed in 4% PFA overnight at 4°C and cleared in methanol. Embryos were mounted in glycerol, and images were captured at RT using DP Capture software (Olympus) on a stereomicroscope (SZX-12; Olympus) with a color camera (DP-71 12 Mp). Raw images were assembled using Photoshop.

MO experiments

An MO antisense oligonucleotide was designed against the following sequence of *cavin-1a* (position −22): 5′-CATGGCTTGGTTTCAAGTAGACTCC-3′. Standard control MO (5′-CCTCTTACCTCAGTTACAATTTATA-3′) was used. MOs were obtained from Gene Tools, LLC and diluted for injection in Danieau's solution (58 mM NaCl, 0.7 mM KCl, 0.4 mM $MgSO_4$, 0.6 mM $Ca(NO_3)_2$, and 5 mM Hepes, pH 7.6) with phenol red as an indicator. *Cavin-1a* or control MO (3 ng/µl) was injected into fertilized eggs from WT, *tp53*^{zdf1} (Berghmans et al., 2005), or *tg(bact2-EGFPcaax)*^{pc10} (Williams et al., 2011) fish lines at the 1–2 cell stage. Live embryos were immobilized in E3 containing tricaine (0.2% 3-aminobenzoic acid ethyl ester), and images were captured on a stereomicroscope (SZX-12) as described in the previous paragraph. Isolation of zebrafish fibers from 5-d-old embryos was performed as previously described (Nixon et al., 2005). Fibers were allowed to settle onto 3-cm Matrigel-coated dishes for 2 h followed by ruthenium red labeling as described in the EM section. To make the *cavin1a-GFP* MO target sequence, we fused the 47 bp 5′ of the ATG of *cavin1a* (which includes the *cavin1a-MO* target sequence) to EGFP. The vector for in vitro transcription was made by recombining p5E-CMV/SP6, p3E-pA, pDEST-Tol2-pA2 (Kwan et al., 2007), and pME-cavin1a-MO control (this study; GenBank accession no. KM211533). mRNA was transcribed using the SP6 mMessage mMachine kit (Ambion) and purified using the MEGAclear kit (Ambion). Images of live embryos in E3 were captured at RT with NIS Elements software (Nikon) on a stereomicroscope (SMZ1500; Nikon) using the GFP filter with a HR Plan Apochromat 1× objective and a camera (CoolSNAP ES2 MonoChrome; Roper Scientific). Raw images were assembled using Photoshop.

Transgenic zebrafish lines

The *tg(cav3:Cav3WT-GFP)*^{uq1rp} and *tg(cav3:Cav3R26Q-GFP)*^{uq2rp} lines were generated using the Tol2 transposon system as previously described (Kawakami, 2007). The cav3:Cav3-GFP construct (Nixon et al., 2009) was subcloned into the Tol2 vector pT2KXIGΔin (Urasaki et al., 2006), and the Cav3-R26Q point mutation was generated via PCR-based mutagenesis. Transposase mRNA was generated from pCS-TP (Kawakami et al., 2004) using mMessage mMachine and purified using the MegaClear kit. Zebrafish embryos at the one-cell stage were coinjected with transposase mRNA/Cav3-GFP plasmid (25 ng/µl each), and GFP-positive embryos were allowed to reach maturity. Founders were identified by outcrossing to WT fish and screening for GFP-positive embryos.

MC and EBD uptake

72-hpf zebrafish embryos were incubated in 3% MC (in E3) for 24 h and then injected with 0.1 mg/ml EBD as previously described (Bassett et al., 2003). After 4–6 h, anesthetized embryos were mounted in 0.7% low melting point agarose, and confocal images were captured as per the immunostaining protocol using a Plan Apochromat 20×/0.8 NA M27 water immersion lens.

Statistical analyses

Statistical analyses were conducted using Excel (Microsoft). Error bars represent means ± SEM unless otherwise noted. P-values were determined using an unpaired Student's *t* test; values less than 0.05 were considered statistically significant.

Online supplemental material

Fig. S1 shows additional images of the ultrastructure of *cavin-1*$^{-/-}$ whole-muscle sections and isolated muscle fibers. Fig. S2 shows mean diameter of caveolae and vacuoles and multilamellar structures in *cavin-1*$^{-/-}$ muscle fibers. Fig. S3 shows additional surface-rendered reconstructions of the honeycomb reticulated networks in *cavin-1*$^{-/-}$

muscle fibers and analysis of T-tubule protein expression in WT and *cavin-1*$^{-/-}$ muscle. Fig. S4 shows nuclear localization of Cavin-4 in *cavin-1*$^{-/-}$ muscle cryosections, electron tomography quantitation of the number of caveolae per rosette after hypo-osmotic treatment, hypo-osmotic treatment of isolated muscle fibers, and relative Cavin-1 expression in WT and Cavin1-GFP–rescued muscle fibers. Fig. S5 shows evolutionary analysis for *D. rerio* Cavin-1a, additional controls and dose–response graph for MO injections, and Western analysis of Cav3-GFP expression in zebrafish embryos. Video 1 shows the four-limb hang test in WT and *cavin-1*$^{-/-}$ mice. Video 2 shows EM tomogram of a WT muscle fiber. Video 3 shows a 3D representation of a WT muscle fiber. Video 4 shows an EM tomogram of a *cavin-1*$^{-/-}$ muscle fiber. Video 5 shows a 3D representation of a *cavin-1*$^{-/-}$ muscle fiber. Video 6 shows an EM tomogram of a WT muscle fiber in iso-osmotic media. Video 7 shows an EM tomogram of a WT muscle fiber in hypo-osmotic media. Video 8 shows a time-lapse of WT and *cavin-1*$^{-/-}$ muscle fibers in a hypo-osmotic medium. Online supplemental material is available at http://www.jcb.org/cgi/content/full/jcb.201501046/DC1.

Acknowledgments

Confocal microscopy was performed at the Australian Cancer Research Foundation (ACRF)/Institute for Molecular Bioscience Dynamic Imaging Facility for Cancer Biology, established with funding from the ACRF. The authors acknowledge the use of the Australian Microscopy & Microanalysis Research Facility at the Center for Microscopy and Microanalysis at The University of Queensland. Molecular graphics images were produced using the UCSF Chimera package from the Resource for Biocomputing, Visualization, and Informatics at the University of California, San Francisco (supported by National Institutes of Health P41 RR001081). We are also grateful to the University of Queensland Major Equipment and Infrastructure Scheme, the Welford Donation, and members of the Parton laboratory for comments on the manuscript. We thank Pascale Koebel (Institut de Génétique et de Biologie Moléculaire et Cellulaire, France) for production of recombinant adeno-associated virus.

This work was supported by grants and a fellowship from the National Health and Medical Research Council of Australia (grant numbers APP1037320, APP1045092, APP1058565, and APP569542 to R.G. Parton) and from the National Institutes of Health (DK30425 and DK56935 to P.F. Pilch).

The authors declare no competing financial interests.

Submitted: 13 January 2015
Accepted: 23 July 2015

References

Bansal, D., K. Miyake, S.S. Vogel, S. Groh, C.C. Chen, R. Williamson, P.L. McNeil, and K.P. Campbell. 2003. Defective membrane repair in dysferlin-deficient muscular dystrophy. *Nature.* 423:168–172. http://dx.doi.org/10.1038/nature01573

Bassett, D.I., R.J. Bryson-Richardson, D.F. Daggett, P. Gautier, D.G. Keenan, and P.D. Currie. 2003. Dystrophin is required for the formation of stable muscle attachments in the zebrafish embryo. *Development.* 130:5851–5860. http://dx.doi.org/10.1242/dev.00799

Bastiani, M., and R.G. Parton. 2010. Caveolae at a glance. *J. Cell Sci.* 123:3831–3836. http://dx.doi.org/10.1242/jcs.070102

Bastiani, M., L. Liu, M.M. Hill, M.P. Jedrychowski, S.J. Nixon, H.P. Lo, D. Abankwa, R. Luetterforst, M. Fernandez-Rojo, M.R. Breen, et al. 2009. MURC/Cavin-4 and cavin family members form tissue-specific caveolar complexes. *J. Cell Biol.* 185:1259–1273. http://dx.doi.org/10.1083/jcb.200903053

Berghmans, S., R.D. Murphey, E. Wienholds, D. Neuberg, J.L. Kutok, C.D. Fletcher, J.P. Morris, T.X. Liu, S. Schulte-Merker, J.P. Kanki, et al. 2005. tp53 mutant zebrafish develop malignant peripheral nerve sheath tumors. *Proc. Natl. Acad. Sci. USA.* 102:407–412. http://dx.doi.org/10.1073/pnas.0406252102

Cai, C., N. Weisleder, J.K. Ko, S. Komazaki, Y. Sunada, M. Nishi, H. Takeshima, and J. Ma. 2009. Membrane repair defects in muscular dystrophy are linked to altered interaction between MG53, caveolin-3, and dysferlin. *J. Biol. Chem.* 284:15894–15902. http://dx.doi.org/10.1074/jbc.M109.009589

Carlson, G. 2011. The use of four limb hanging tests to monitor muscle strength and condition over time. Available at: http://www.treat-nmd.eu/downloads/file/sops/dmd/MDX/DMD_M.2.1.005.pdf (accessed August 3, 2015)

Corrotte, M., P.E. Almeida, C. Tam, T. Castro-Gomes, M.C. Fernandes, B.A. Millis, M. Cortez, H. Miller, W. Song, T.K. Maugel, and N.W. Andrews. 2013. Caveolae internalization repairs wounded cells and muscle fibers. *eLife.* 2:e00926. http://dx.doi.org/10.7554/eLife.00926

Cowling, B.S., A. Toussaint, L. Amoasii, P. Koebel, A. Ferry, L. Davignon, I. Nishino, J.L. Mandel, and J. Laporte. 2011. Increased expression of wild-type or a centronuclear myopathy mutant of dynamin 2 in skeletal muscle of adult mice leads to structural defects and muscle weakness. *Am. J. Pathol.* 178:2224–2235. http://dx.doi.org/10.1016/j.ajpath.2011.01.054

Deacon, R.M. 2013. Measuring the strength of mice. *J. Vis. Exp.* 76.

Dulhunty, A.F., and C. Franzini-Armstrong. 1975. The relative contributions of the folds and caveolae to the surface membrane of frog skeletal muscle fibres at different sarcomere lengths. *J. Physiol.* 250:513–539. http://dx.doi.org/10.1113/jphysiol.1975.sp011068

Galbiati, F., J.A. Engelman, D. Volonte, X.L. Zhang, C. Minetti, M. Li, H. Hou Jr., B. Kneitz, W. Edelmann, and M.P. Lisanti. 2001. Caveolin-3 null mice show a loss of caveolae, changes in the microdomain distribution of the dystrophin-glycoprotein complex, and t-tubule abnormalities. *J. Biol. Chem.* 276:21425–21433. http://dx.doi.org/10.1074/jbc.M100828200

Gambin, Y., N. Ariotti, K.A. McMahon, M. Bastiani, E. Sierecki, O. Kovtun, M.E. Polinkovsky, A. Magenau, W. Jung, S. Okano, et al. 2014. Single-molecule analysis reveals self assembly and nanoscale segregation of two distinct cavin subcomplexes on caveolae. *eLife.* 3:e01434. http://dx.doi.org/10.7554/eLife.01434

Griffiths, G., R. Back, and M. Marsh. 1989. A quantitative analysis of the endocytic pathway in baby hamster kidney cells. *J. Cell Biol.* 109:2703–2720. http://dx.doi.org/10.1083/jcb.109.6.2703

Hall, T.E., R.J. Bryson-Richardson, S. Berger, A.S. Jacoby, N.J. Cole, G.E. Hollway, J. Berger, and P.D. Currie. 2007. The zebrafish candyfloss mutant implicates extracellular matrix adhesion failure in laminin alpha2-deficient congenital muscular dystrophy. *Proc. Natl. Acad. Sci. USA.* 104:7092–7097. http://dx.doi.org/10.1073/pnas.0700942104

Hansen, C.G., E. Shvets, G. Howard, K. Riento, and B.J. Nichols. 2013. Deletion of cavin genes reveals tissue-specific mechanisms for morphogenesis of endothelial caveolae. *Nat. Commun.* 4:1831. http://dx.doi.org/10.1038/ncomms2808

Hayashi, Y.K., C. Matsuda, M. Ogawa, K. Goto, K. Tominaga, S. Mitsuhashi, Y.E. Park, I. Nonaka, N. Hino-Fukuyo, K. Haginoya, et al. 2009. Human PTRF mutations cause secondary deficiency of caveolins resulting in muscular dystrophy with generalized lipodystrophy. *J. Clin. Invest.* 119:2623–2633. http://dx.doi.org/10.1172/JCI38660

Hill, M.M., M. Bastiani, R. Luetterforst, M. Kirkham, A. Kirkham, S.J. Nixon, P. Walser, D. Abankwa, V.M. Oorschot, S. Martin, et al. 2008. PTRF-Cavin, a conserved cytoplasmic protein required for caveola formation and function. *Cell.* 132:113–124. http://dx.doi.org/10.1016/j.cell.2007.11.042

Kawakami, K. 2007. Tol2: a versatile gene transfer vector in vertebrates. *Genome Biol.* 8(Suppl. 1):S7. http://dx.doi.org/10.1186/gb-2007-8-s1-s7

Kawakami, K., H. Takeda, N. Kawakami, M. Kobayashi, N. Matsuda, and M. Mishina. 2004. A transposon-mediated gene trap approach identifies developmentally regulated genes in zebrafish. *Dev. Cell.* 7:133–144. http://dx.doi.org/10.1016/j.devcel.2004.06.005

Kozera, L., E. White, and S. Calaghan. 2009. Caveolae act as membrane reserves which limit mechanosensitive I(Cl,swell) channel activation during swelling in the rat ventricular myocyte. *PLoS ONE.* 4:e8312. http://dx.doi.org/10.1371/journal.pone.0008312

Kremer, J.R., D.N. Mastronarde, and J.R. McIntosh. 1996. Computer visualization of three-dimensional image data using IMOD. *J. Struct. Biol.* 116:71–76. http://dx.doi.org/10.1006/jsbi.1996.0013

Kwan, K.M., E. Fujimoto, C. Grabher, B.D. Mangum, M.E. Hardy, D.S. Campbell, J.M. Parant, H.J. Yost, J.P. Kanki, and C.B. Chien. 2007. The Tol2kit: a multisite gateway-based construction kit for Tol2 transposon transgenesis constructs. *Dev. Dyn.* 236:3088–3099. http://dx.doi.org/10.1002/dvdy.21343

Lamb, G.D. 2005. Rippling muscle disease may be caused by "silent" action potentials in the tubular system of skeletal muscle fibers. *Muscle Nerve.* 31:652–658. http://dx.doi.org/10.1002/mus.20307

Liu, L., and P.F. Pilch. 2008b. A critical role of cavin (polymerase I and transcript release factor) in caveolae formation and organization. *J. Biol. Chem.* 283:4314–4322. http://dx.doi.org/10.1074/jbc.M707890200

Liu, L., D. Brown, M. McKee, N.K. Lebrasseur, D. Yang, K.H. Albrecht, K. Ravid, and P.F. Pilch. 2008a. Deletion of Cavin/PTRF causes global loss of caveolae, dyslipidemia, and glucose intolerance. *Cell Metab.* 8:310–317. http://dx.doi.org/10.1016/j.cmet.2008.07.008

Martin, S., M.A. Fernandez-Rojo, A.C. Stanley, M. Bastiani, S. Okano, S.J. Nixon, G. Thomas, J.L. Stow, and R.G. Parton. 2012. Caveolin-1 deficiency leads to increased susceptibility to cell death and fibrosis in white adipose tissue: characterization of a lipodystrophic model. *PLoS ONE.* 7:e46242. http://dx.doi.org/10.1371/journal.pone.0046242

Mastronarde, D.N. 2005. Automated electron microscope tomography using robust prediction of specimen movements. *J. Struct. Biol.* 152:36–51. http://dx.doi.org/10.1016/j.jsb.2005.07.007

Matsuda, C., Y.K. Hayashi, M. Ogawa, M. Aoki, K. Murayama, I. Nishino, I. Nonaka, K. Arahata, and R.H. Brown Jr. 2001. The sarcolemmal proteins dysferlin and caveolin-3 interact in skeletal muscle. *Hum. Mol. Genet.* 10:1761–1766. http://dx.doi.org/10.1093/hmg/10.17.1761

Minetti, C., M. Bado, P. Broda, F. Sotgia, C. Bruno, F. Galbiati, D. Volonte, G. Lucania, A. Pavan, E. Bonilla, et al. 2002. Impairment of caveolae formation and T-system disorganization in human muscular dystrophy with caveolin-3 deficiency. *Am. J. Pathol.* 160:265–270. http://dx.doi.org/10.1016/S0002-9440(10)64370-2

Nguyen, J.V., I. Soto, K.Y. Kim, E.A. Bushong, E. Oglesby, F.J. Valiente-Soriano, Z. Yang, C.H. Davis, J.L. Bedont, J.L. Son, et al. 2011. Myelination transition zone astrocytes are constitutively phagocytic and have synuclein dependent reactivity in glaucoma. *Proc. Natl. Acad. Sci. USA.* 108:1176–1181. http://dx.doi.org/10.1073/pnas.1013965108

Nixon, S.J., J. Wegner, C. Ferguson, P.F. Méry, J.F. Hancock, P.D. Currie, B. Key, M. Westerfield, and R.G. Parton. 2005. Zebrafish as a model for caveolin-associated muscle disease; caveolin-3 is required for myofibril organization and muscle cell patterning. *Hum. Mol. Genet.* 14:1727–1743. http://dx.doi.org/10.1093/hmg/ddi179

Nixon, S.J., R.I. Webb, M. Floetenmeyer, N. Schieber, H.P. Lo, and R.G. Parton. 2009. A single method for cryofixation and correlative light, electron microscopy and tomography of zebrafish embryos. *Traffic.* 10:131–136. http://dx.doi.org/10.1111/j.1600-0854.2008.00859.x

Noske, A.B., A.J. Costin, G.P. Morgan, and B.J. Marsh. 2008. Expedited approaches to whole cell electron tomography and organelle mark-up in situ in high-pressure frozen pancreatic islets. *J. Struct. Biol.* 161:298–313. http://dx.doi.org/10.1016/j.jsb.2007.09.015

Ogata, T., T. Ueyama, K. Isodono, M. Tagawa, N. Takehara, T. Kawashima, K. Harada, T. Takahashi, T. Shioi, H. Matsubara, and H. Oh. 2008. MURC, a muscle-restricted coiled-coil protein that modulates the Rho/ROCK pathway, induces cardiac dysfunction and conduction disturbance. *Mol. Cell. Biol.* 28:3424–3436. http://dx.doi.org/10.1128/MCB.02186-07

Ogata, T., D. Naito, N. Nakanishi, Y.K. Hayashi, T. Taniguchi, K. Miyagawa, T. Hamaoka, N. Maruyama, S. Matoba, K. Ikeda, et al. 2014. MURC/Cavin-4 facilitates recruitment of ERK to caveolae and concentric cardiac hypertrophy induced by α1-adrenergic receptors. *Proc. Natl. Acad. Sci. USA.* 111:3811–3816. http://dx.doi.org/10.1073/pnas.1315359111

Parton, R.G. 1994. Ultrastructural localization of gangliosides; GM1 is concentrated in caveolae. *J. Histochem. Cytochem.* 42:155–166. http://dx.doi.org/10.1177/42.2.8288861

Parton, R.G., and M.A. del Pozo. 2013. Caveolae as plasma membrane sensors, protectors and organizers. *Nat. Rev. Mol. Cell Biol.* 14:98–112. http://dx.doi.org/10.1038/nrm3512

Parton, R.G., M. Way, N. Zorzi, and E. Stang. 1997. Caveolin-3 associates with developing T-tubules during muscle differentiation. *J. Cell Biol.* 136:137–154. http://dx.doi.org/10.1083/jcb.136.1.137

Parton, R.G., J.C. Molero, M. Floetenmeyer, K.M. Green, and D.E. James. 2002. Characterization of a distinct plasma membrane macrodomain in differentiated adipocytes. *J. Biol. Chem.* 277:46769–46778. http://dx.doi.org/10.1074/jbc.M205683200

Pearen, M.A., N.A. Eriksson, R.L. Fitzsimmons, J.M. Goode, N. Martel, S. Andrikopoulos, and G.E. Muscat. 2012. The nuclear receptor, Nor-1, markedly increases type II oxidative muscle fibers and resistance to fatigue. *Mol. Endocrinol.* 26:372–384. http://dx.doi.org/10.1210/me.2011-1274

Rahkila, P., A. Alakangas, K. Väänänen, and K. Metsikkö. 1996. Transport pathway, maturation, and targetting of the vesicular stomatitis virus glycoprotein in skeletal muscle fibers. *J. Cell Sci.* 109:1585–1596.

Rajab, A., V. Straub, L.J. McCann, D. Seelow, R. Varon, R. Barresi, A. Schulze, B. Lucke, S. Lützkendorf, M. Karbasiyan, et al. 2010. Fatal cardiac arrhythmia and long-QT syndrome in a new form of congenital generalized lipodystrophy with muscle rippling (CGL4) due to PTRF-CAVIN mutations. *PLoS Genet.* 6:e1000874. http://dx.doi.org/10.1371/journal.pgen.1000874

Ravenscroft, G., K.J. Nowak, C. Jackaman, S. Clément, M.A. Lyons, S. Gallagher, A.J. Bakker, and N.G. Laing. 2007. Dissociated flexor digitorum brevis myofiber culture system—a more mature muscle culture system. *Cell Motil. Cytoskeleton.* 64:727–738. http://dx.doi.org/10.1002/cm.20223

Rayns, D.G., F.O. Simpson, and W.S. Bertaud. 1968. Surface features of striated muscle. II. Guinea-pig skeletal muscle. *J. Cell Sci.* 3:475–482.

Richter, T., M. Floetenmeyer, C. Ferguson, J. Galea, J. Goh, M.R. Lindsay, G.P. Morgan, B.J. Marsh, and R.G. Parton. 2008. High-resolution 3D quantitative analysis of caveolar ultrastructure and caveola-cytoskeleton interactions. *Traffic.* 9:893–909. http://dx.doi.org/10.1111/j.1600-0854.2008.00733.x

Robu, M.E., J.D. Larson, A. Nasevicius, S. Beiraghi, C. Brenner, S.A. Farber, and S.C. Ekker. 2007. p53 activation by knockdown technologies. *PLoS Genet.* 3:e78. http://dx.doi.org/10.1371/journal.pgen.0030078

Rodriguez, G., T. Ueyama, T. Ogata, G. Czernuszewicz, Y. Tan, G.W. Dorn II, R. Bogaev, K. Amano, H. Oh, H. Matsubara, et al. 2011. Molecular genetic and functional characterization implicate muscle-restricted coiled-coil gene (MURC) as a causal gene for familial dilated cardiomyopathy. *Circ Cardiovasc Genet.* 4:349–358. http://dx.doi.org/10.1161/CIRCGENETICS.111.959866

Sinha, B., D. Köster, R. Ruez, P. Gonnord, M. Bastiani, D. Abankwa, R.V. Stan, G. Butler-Browne, B. Vedie, L. Johannes, et al. 2011. Cells respond to mechanical stress by rapid disassembly of caveolae. *Cell.* 144:402–413. http://dx.doi.org/10.1016/j.cell.2010.12.031

Söderberg, O., K.J. Leuchowius, M. Gullberg, M. Jarvius, I. Weibrecht, L.G. Larsson, and U. Landegren. 2008. Characterizing proteins and their interactions in cells and tissues using the in situ proximity ligation assay. *Methods.* 45:227–232. http://dx.doi.org/10.1016/j.ymeth.2008.06.014

Sotgia, F., S.E. Woodman, G. Bonuccelli, F. Capozza, C. Minetti, P.E. Scherer, and M.P. Lisanti. 2003. Phenotypic behavior of caveolin-3 R26Q, a mutant associated with hyperCKemia, distal myopathy, and rippling muscle disease. *Am. J. Physiol. Cell Physiol.* 285:C1150–C1160. http://dx.doi.org/10.1152/ajpcell.00166.2003

Thisse, C., B. Thisse, T.F. Schilling, and J.H. Postlethwait. 1993. Structure of the zebrafish snail1 gene and its expression in wild-type, spadetail and no tail mutant embryos. *Development.* 119:1203–1215.

Urasaki, A., G. Morvan, and K. Kawakami. 2006. Functional dissection of the Tol2 transposable element identified the minimal cis-sequence and a highly repetitive sequence in the subterminal region essential for transposition. *Genetics.* 174:639–649. http://dx.doi.org/10.1534/genetics.106.060244

Wang, X., N. Weisleder, C. Collet, J. Zhou, Y. Chu, Y. Hirata, X. Zhao, Z. Pan, M. Brotto, H. Cheng, and J. Ma. 2005. Uncontrolled calcium sparks act as a dystrophic signal for mammalian skeletal muscle. *Nat. Cell Biol.* 7:525–530. http://dx.doi.org/10.1038/ncb1254

Way, M., and R.G. Parton. 1995. M-caveolin, a muscle-specific caveolin-related protein. *FEBS Lett.* 376:108–112. http://dx.doi.org/10.1016/0014-5793(95)01256-7

Weibel, E.R. 1979. Stereological Methods: Practical Methods for Biological Morphometry. Vol. 1. Academic Press, New York. 415 pp.

Williams, R.J., T.E. Hall, V. Glattauer, J. White, P.J. Pasic, A.B. Sorensen, L. Waddington, K.M. McLean, P.D. Currie, and P.G. Hartley. 2011. The in vivo performance of an enzyme-assisted self-assembled peptide/protein hydrogel. *Biomaterials.* 32:5304–5310. http://dx.doi.org/10.1016/j.biomaterials.2011.03.078

Woodman, S.E., F. Sotgia, F. Galbiati, C. Minetti, and M.P. Lisanti. 2004. Caveolinopathies: mutations in caveolin-3 cause four distinct autosomal dominant muscle diseases. *Neurology.* 62:538–543. http://dx.doi.org/10.1212/WNL.62.4.538

Zhu, H., P. Lin, G. De, K.H. Choi, H. Takeshima, N. Weisleder, and J. Ma. 2011. Polymerase transcriptase release factor (PTRF) anchors MG53 protein to cell injury site for initiation of membrane repair. *J. Biol. Chem.* 286:12820–12824. http://dx.doi.org/10.1074/jbc.C111.221440